Delft University of Technology

A local eddy viscosity parameterization for wind-driven estuarine exchange flow, Part II Entrainment

Basdurak, N. Berkay; Burchard, Hans; Schuttelaars, Henk M.

DOI
10.1016/j.pocean.2023.103166

Publication date
2023

Document Version
Final published version

Published in
Progress in Oceanography

Citation (APA)
Basdurak, N. B., Burchard, H., & Schuttelaars, H. M. (2023). A local eddy viscosity parameterization for wind-driven estuarine exchange flow, Part II: Entrainment. *Progress in Oceanography*, *219*, Article 103166. https://doi.org/10.1016/j.pocean.2023.103166

Progress in Oceanography 219 (2023) 103166

Contents lists available at ScienceDirect

Progress in Oceanography

journal homepage: www.elsevier.com/locate/pocean

A local eddy viscosity parameterization for wind-driven estuarine exchange flow, Part II: Entrainment

N. Berkay Basdurak [a,b,*], Hans Burchard [a], Henk M. Schuttelaars [c]

[a] Leibniz Institute for Baltic Sea Research Warnemünde, Seestr. 15, D-18119, Rostock, Germany
[b] Institute of Marine Sciences, Middle East Technical University, Erdemli 33731, Turkey
[c] Delft Institute of Applied Mathematics, Delft University of Technology, Delft, Netherlands

ARTICLE INFO

Keywords:
Wind driven exchange flow
Eddy viscosity parameterization
Estuarine dynamics
Analytical techniques
Boundary layer mixing
Wind entrainment

ABSTRACT

Structure and intensity of estuarine exchange flow depend significantly on the eddy viscosity A_v profile which is dynamically linked to various forces (e.g., gravitational, tidal, wind-driven). The impact of winds on the exchange flow is complex due to its direct (local and remote changes in shear and density stratification) and indirect (modifications to A_v profiles) contributions. This study aims (i) to include wind entrainment effects in the tidally averaged A_v parameterization; (ii) to develop an analytical one-dimensional model for the wind driven exchange flow by using this novel parameterization and assess the tidally averaged dynamics over a relevant physical parameter-space, subdomains of which have not yet been explored numerically. This one-dimensional model is based on a balance between frictional forces and pressure gradient, calibrated with a tidally-resolving one-dimensional water-column model with second-moment closure. Structure and intensity of the resulting exchange flow profiles are analyzed with respect to three dimensionless parameters (the unsteadiness of boundary layer mixing U_n, scaled-directional wind stress W, and horizontal stratification S_i). While down-estuarine winds enhance the gravitational circulation, up-estuarine winds result in either a two-layer inverted circulation opposing the gravitational circulation, or a three-layer flow (favored by relatively strong S_i, weak W, and moderate U_n) that is up-estuarine at the surface with classical two-layer circulation underneath. Relative thickness of surface and bottom boundary layers affect both the intensity and the inflection depth of the exchange flow layers. Up-estuarine winds with $W \gtrsim 0.5$ yield unstable stratification and reduce the exchange flow intensity with increasing W.

1. Introduction

The exchange flow is the tidally-averaged estuarine circulation in along-channel direction, commonly observed as a bidirectional flow with an up-estuarine salty layer overlaid by a down-estuarine freshwater layer. For a given bathymetry, the shape and magnitude of this flow depend significantly on the various forcings (e.g., tides, river discharge, wind) and the associated eddy viscosity profiles at various time scales. While the temporal variations in the eddy viscosity profiles contribute indirectly to the exchange flow via tidally and gravitationally (Burchard et al., 2011; Cheng et al., 2011, 2013; Dijkstra et al., 2017) driven eddy viscosity shear covariance (ESCO), the tidally averaged eddy viscosity profile also directly impacts the exchange flow (Burchard and Hetland, 2010).

The impact of wind on the exchange flow is much less studied compared to the influence of tidal forcing. Wind affects the stability of the water column and the resulting flow fields directly (local changes in density-stratification due to directional wind mixing and straining; remote unidirectional changes in the flow shear and slope of the buoyancy gradient) and indirectly by altering the eddy viscosity profiles. The latter results from the changes in shear and density stratification. Focusing on the effect of directional wind stress on stratification, various observational and numerical studies have reported on down-estuarine winds enhancing stratification and up-estuarine winds suppressing it (Scully et al., 2005; Burchard, 2009; Verspecht et al., 2009). However, Chen and Sanford (2009) found an increase-then-decrease transition with increasing down-estuary wind shear. By using an analytical model, Jongbloed et al. (2022) has recently argued that both these monotone and alternating responses can be explained in terms of dominant salt balances.

The exchange flow profiles themselves also depend strongly on the wind effects. Numerical models show that directional winds can alter the commonly observed two-layered exchange flow with down-estuary winds enhancing it (Chen and Sanford, 2009; Burchard and

---

[*] Corresponding author at: Institute of Marine Sciences, Middle East Technical University, Erdemli 33731, Turkey.
E-mail addresses: berkay.basdurak@io-warnemuende.de, berkay@ims.metu.edu.tr (N.B. Basdurak).

https://doi.org/10.1016/j.pocean.2023.103166
Received 17 July 2023; Received in revised form 5 October 2023; Accepted 1 November 2023

Hetland, 2010) and up-estuary winds suppressing and even inverting it (Lange and Burchard, 2019). Numerical models depending on second-order closure schemes for the eddy viscosity offer a valuable insight into wind-driven dynamics. However use of these models also has some drawbacks: column models driven by horizontal density gradients often perform poorly in weakly turbulent mixing regimes yielding non-physical high stratification i.e., runaway stratification, and idealized 3D models with stratification dependent mixing closures tend towards runaway stratification when the mixing in the pycnocline is reduced to its background levels (Hetland and Geyer, 2004). Recently Burchard et al. (2023) have avoided runaway stratification in their tidally enforced column model simulations by nudging salinity to a constant background salinity for strongly stable stratification while preserving tidal periodicity, thus extended the physical parameter space that can be explored by column models. However, compared to complex numerical models, analytical models can allow for sensitivity studies over a wider range of physical parameter space and in that parameterization of eddy viscosity profiles is crucial.

Most analytical models that have been developed adopt simplified eddy viscosity profiles e.g., uniform (Jongbloed et al., 2022) or parabolic (Zitman and Schuttelaars, 2012) shapes. The analytical model of Chen and De Swart (2016) uses an eddy viscosity parameterization that deviates from a parabolic shape to include the bottom boundary layer effect. Recently we have developed a tidally averaged eddy viscosity parameterization that considers the influence of vertical stratification interacting with the along channel buoyancy gradient through the change of the bottom boundary layer (BBL) thickness, and depending on the wind stress at the surface (Basdurak et al., 2021). Other studies including both experimental (Kato and Phillips, 1969; Price, 1979) and numerical (Deleersnijder and Luyten, 1994; Burchard et al., 1998) ones, focus only on the surface boundary layer (SBL) due to wind entrainment (i.e., wind stress is the only source of turbulence and the SBL grows in time). All aforementioned parameterizations consider either the BBL or the SBL. Such simplifications result from the lack of a physically motivated eddy viscosity parameterization that includes the boundary layer characteristics due to wind entrainment, and interaction of surface and bottom boundary layers in stratified fluids.

In view of the aforementioned knowledge gap, the aim of this study is two-fold: (I) to extend the tidally averaged eddy viscosity parameterization introduced in Basdurak et al. (2021) by including wind entrainment effects and to analyze the relation between the interacting boundary layers, (II) to develop an analytical model for the wind driven exchange flow by using this novel parameterization and assess the tidally averaged dynamics over a relevant physical parameter-space, subdomains of which have not yet been explored numerically. To achieve the first aim, the complex interaction of directional-wind and stratification needs to be accurately captured in the parameterized eddy viscosity profile. We use the tidally-averaged result of a 1D numerical model that is tidally-resolving column-model with second-moment closure together with available observational and theoretical findings to derive relations for tidally averaged boundary layer thicknesses in terms of three dimensionless parameters: the unsteadiness of boundary layer mixing, scaled-directional wind stress, and vertical stratification that is related to horizontal stratification. These relations allow us to parameterize the tidally averaged eddy viscosity profile. Since the dimensionless parameters defining the eddy viscosity profile only depend on simple local characteristics (e.g., water column depth, wind stress, density profile, surface and bottom roughnesses, and tidal velocity-amplitude and frequency), the parameterization can be used directly to estimate the structure of tidally averaged eddy viscosity profiles for these in-situ parameters. The parameterization is calibrated with the column-model for the subrange of stratification and avoiding runaway stratification by relaxing the salinity time-scales; the range of parameter space that is used for calibration is chosen iteratively such that the parameters are varied around the points of periodic solution yielding a wide range of unsteadiness, rather than exploring a fixed range which can lead to a narrow band of numerical solutions. Using vertical and horizontal stratification bounds (that are derived from the findings of sheared direct numerical simulations, lab experiments and observational estuarine studies, see Basdurak et al., 2021), allows for an investigation of the dynamic link between the tidally-averaged characteristics of the parameterized eddy viscosity profiles and boundary layers (thus local characteristics) over a wider range of physical parameter space. The second aim is achieved by using the parameterized eddy viscosity profile to solve the one-dimensional tidally-averaged dynamic equation for the exchange flow. This approach allows for the study of the sensitivity of exchange flow profiles to the dimensionless parameters.

The remainder of this paper is organized as follows. In Section 2, we show the dynamical equation and introduce the new eddy viscosity parameterization. In Section 3, we derive tidally-averaged relations for wind-adjusted stratification and boundary layer thicknesses in terms of state parameters using a 1D numerical model; local maxima locations and magnitudes of eddy viscosity profiles are related to boundary layer thicknesses and dimensionless parameters, respectively; sensitivity of the parameterization over the dimensionless parameter space is shown. In Section 4, exchange flow profiles resulting from the analytical model are compared to the ones resulting from the numerical model over a three dimensional parameter space. In Section 5, the exchange flow intensity and the inflection depth (depth where flow changes direction) is discussed in relation to boundary layer thicknesses and runoff velocity. A comparison between the analytical and numerical model is shown for the exchange flow intensities. The main findings are summarized in Section 6.

2. Model description

2.1. Dynamical equation

By ignoring earth's rotation and advection the one-dimensional, uniform in along-channel direction, tidally-averaged momentum equation reduces to a balance between pressure gradient and friction:

$$\partial_z \left(A_v \partial_z u\right) = z\partial_x b + p_x/\rho_0\,, \quad -H \le z \le 0, \tag{1}$$

with all physical variables tidally averaged (thus ignoring the contribution from ESCO). The longitudinal and upward Cartesian coordinates are denoted by x and z, respectively. The water depth is given by H. The buoyancy is defined as $b = -g\left(\rho-\rho_0\right)/\rho_0$ with the reference density $\rho_0 = 1000$ kg m^{-3} and $g = 9.81$ m s^{-2} is the gravitational acceleration. The eddy viscosity is denoted by A_v. The surface slope driven external pressure gradient p_x is obtained through the constraint $\int_{-H}^{0} u(z)\,dz = Hu_r$ (Burchard and Hetland, 2010) with u_r the prescribed residual depth-mean velocity. Boundary conditions are a no-slip condition at the bottom, $u(z=-H)=0$, and a prescribed momentum flux at the surface $A_v\partial_z u(z=0) = \tau^s/\rho_0 = u_*^s|u_*^s|$ where τ^s denotes the wind stress, positive in up-estuarine direction $\tau^s > 0$ and negative in down-estuarine direction $\tau^s < 0$ (Lange and Burchard, 2019), with the surface friction velocity u_*^s.

2.2. Nondimensional parameters

The momentum equation is made non-dimensional by introducing the following variables:

$$\tilde z = \frac{z}{H}, \quad (\tilde u, \tilde u_r) = \frac{(u, u_r)}{\left|u_*^b\right|}, \quad \tilde A_v = \frac{A_v}{\left|u_*^b\right| H}, \quad \tilde p_x = \frac{p_x}{\rho_0\left(u_*^b\right)^2/H}, \tag{2}$$

where $\tilde p_x$ is a function of $\tilde u_r$. The bottom friction velocity u_*^b is given by

$$(u_*^b)^2 = \frac{\tau^b}{\rho_0} \approx U_T^2 C_D \cong U_T^2\left[\frac{\kappa/f\left(R_i^0\right)}{\left(\tilde z_0^b+1\right)\ln\left(1/\tilde z_0^b+1\right)-1}\right]^2, \tag{3}$$

with $\kappa = 0.41$ the van Kármán constant, and U_T the tidal current amplitude. The drag coefficient C_D depends on the bottom roughness length z_0^b and the bulk Richardson number $R_i^0 = \left(g\Delta\rho/\rho_0\right)/\left(U_T^2/H\right)$, with $\Delta\rho$ the density difference between bottom and surface. The function $f(R_i^0) = 1 + 0.76\kappa\sqrt{R_i^0}$, motivated in Basdurak et al. (2021), is larger than 1 for vertically stratified conditions and equals 1 for well-mixed conditions. In its scaled form (1) can be expressed with the boundary conditions as

$$\partial_{\tilde z}\left(\tilde A_v \partial_{\tilde z}\tilde u\right) = \tilde z S_i + \tilde p_x\,, \quad -1 \le \tilde z \le 0, \tag{4a}$$

$$\tilde A_v \partial_{\tilde z}\tilde u\Big|_{\tilde z=0} = W, \quad \tilde u(\tilde z = -1) = 0, \tag{4b}$$

with Simpson number $S_i = H^2\partial_x b/\left(u_*^b\right)^2$, the ratio of stratifying shear to destratifying mixing (Simpson et al., 1990; Stacey et al., 2010; Burchard et al., 2011). In (4b), $W = W_e \cdot S_i = u_*^s\left|u_*^s\right|/\left(u_*^b\right)^2$ denotes the scaled directional wind stress i.e., the ratio of the surface stress to the bottom stress (Lange and Burchard, 2019; Basdurak et al., 2021). Here, the local Wedderburn number, $W_e = u_*^s\left|u_*^s\right|/(H^2\partial_x b)$, is a measure for relative contributions of wind stress and density-driven forcing on estuarine circulation (Geyer, 1997; Purkiani et al., 2016).

The shape of $\tilde A_v$ depends on two more independent parameters. One is the unsteadiness number $U_n = \omega H/|u_*^b|$, a measure for the importance of unsteadiness of boundary layer mixing (Burchard and Hetland, 2010)with the tidal frequency $\omega = 2\pi/T$ and the tidal period T. Although the model is tidally-averaged, the shape and magnitude of the A_v profiles vary asymmetrically on the tidal time scales tides before being tidally averaged. Thus, the estuarine tidal velocity amplitude, given in (3), plays a role in influencing the boundary layer thicknesses and characterizing the exchange flow.

Another independent parameter that indirectly affects $\tilde u$ is the conjoined impact of vertical stratification and surface shear. In case of no wind entrainment, these effects can be well captured by using the estuarine bulk Richardson number, R_i^0 (Basdurak et al., 2021). However, when wind entrainment is considered, quantifying vertical stratification via R_i^0 may result in under/over-estimates due to: (I) tidal velocity amplitude scaled by the water depth is not sufficient to depict the wind adjusted shear, (II) surface to bottom buoyancy frequency difference ignores the internal changes in stratification. The scaled potential energy anomaly better captures the effects of vertical stratification, because potential energy anomaly ϕ is based on energetic arguments rather than on the top to bottom density difference; ϕ is defined as

$$\phi = \frac{\rho_0}{H}\int_{-H}^{0} z(b - \langle b\rangle)dz \quad , \quad \text{with } \langle b\rangle = \frac{1}{H}\int_{-H}^{0} b\,dz \tag{5}$$

where angular brackets denote depth-averaging. Scaling the potential energy anomaly by $\rho_0 S_i (u_*^b)^2$, Burchard (2009) introduced a dimensionless measure for the degree of vertical stratification. To reduce the dimensionless space, first we adopt an alternative dimensionless form $\tilde\phi = \phi/[\rho_0 (u_*^b)^2]$ which is independent of S_i, then derive a new relation for the wind adjusted bulk Richardson number R_i as a function of $\tilde\phi$ and W using a numerical model. This results in an explicit expression for $R_i(W, \tilde\phi)$ (detailed in Appendix B) including the information of the internal structure of the water column. Thus, the relevant state parameters are W, U_n S_i and R_i. This four dimensional parameter space will be further reduced by relating S_i to R_i (Appendix B).

2.3. Eddy viscosity parameterization

In the absence of wind induced surface entrainment, a two-layer tidally averaged eddy viscosity profile is introduced in Basdurak et al. (2021). The possible effects of stratification in the upper layer are included by the dependency of this profile on R_i (Fig. 1a). In case of wind entrainment, due to the directional wind stress and its complex interaction with stratification, a three-layer eddy viscosity profile can occur with an interfacial layer A_v^I (a band with a relatively strong stratification) separating the two wall layers, denoted as the surface (A_v^S) and the bottom layer (A_v^L); see Fig. 1b–d (blue and green lines, respectively). In case of significant wind forcing, an unstably-stratified tidally averaged conditions may emerge yielding a fully-mixed water column with parabolic shape (Fig. 1f). This profile is analogous to an unstratified water column with no surface-entrainment (Fig. 1e). Thus, a conditionally-layered approach is taken to capture the complex depth-dependent structure of the tidally averaged eddy viscosity profiles described in Fig. 1. The continuous-in-depth and differentiable eddy viscosity A_v reads:

$$A_v = \begin{cases} A_v^L, & -H \le z \le z_L, \\ A_v^I, & z_L \le z \le z_U, \\ A_v^S, & z_U \le z \le 0, \end{cases} \tag{6}$$

with z_L the location of lower maximum in the eddy viscosity profile, and z_U the upper maximum (i.e., the locations where $\partial_z A_v = 0$). With two-local maxima the eddy viscosity profile is three-layered (Fig. 1c–d). If there is only one maximum (as in Fig. 1a–b, e–f) $z_L = z_U$ and the intermediate layer disappears, resulting in a two-layer eddy viscosity profile. Note that the upper layer A_v^U indicates the layer above the BBL maximum, $z_L \le z \le 0$. The expression A_v^L for $-H \le z \le z_L$ is similar to the one in Basdurak et al. (2021) and reads

$$A_v^L = \kappa\left|u_*^b\right|\left(H + z + z_0^b\right)\left(1 - \frac{z + H}{2z_L + 2H + z_0^b} - d_0\right). \tag{7}$$

Note that the log–law of the wall is preserved as the profile is parabolic near the bottom resulting in $A_v^L(-H) = \kappa|u_*^b|z_0^b$ for $d_0 = 0$ (Fig. 1a–e) and $A_v^L(-H) = \kappa(|u_*^b| + |u_*^s|)z_0^b/2$ for $d_0 > 0$ (Fig. 1f). The local maximum of (7) is adjusted by including the coefficient $d_0 \approx (1 - u_*^s/u_*^b)/2$ (Appendix A.2); the coefficient d_0 varies within a range of $0 \le d_0 < 0.5$ (i.e., A_v^L is always positive). This adjustment is necessary because the surface shear dictates the magnitude of the local A_v maximum when up-estuarine winds fully mix the water column i.e., $z_L = -H/2$. Because z_0^b is considerably small relative to H, the A_v maximum equals $\kappa u_*^s H/4$ when $d_0 > 0$ and $\kappa u_*^b H/4$ when $d_0 = 0$. The conditions (up-estuarine winds with a fully-mixed water column) that allow for $d_0 > 0$ are based on the GOTM simulations and will be discussed in the following Section; $d_0 = 0$ otherwise. To complete (6) a conditional expression for A_v^S and A_v^I is developed in Appendix A; it captures the influence of (i) merging boundary layers (the SBL and the BBL fully merge into each other, Fig. 1c, f; the BBL fully merge into SBL, Type I in Fig. 1d) and separated boundary layers (Type II in Fig. 1d), (ii) single layer mixing (the BBL mixing Fig. 1a; the SBL mixing Fig. 1b) on the A_v profiles. The conditional expression depends on the dimensionless parameters defined in the previous section and on the locations z_U and z_L with the corresponding magnitudes of A_v (i.e., f_s and f_b; see Fig. 1 for definitions of these parameters). In the following section, the dependency of these quantities on the dimensionless parameters (defined in the previous sub-section) will be derived and physically motivated.

3. Analytical model development and validation

To complete the tidally-averaged A_v parameterization, its characteristic length scales (z_U, z_L) and its local-maxima magnitudes (f_s, f_b) need to be determined in terms of the state parameters: W, R_i, and U_n. To achieve this, the one-dimensional tide-resolving water column model GOTM (General Ocean Turbulence Model, http://www.gotm.net) consisting of a $k - \varepsilon$ model with algebraic second-moment closure (Umlauf and Burchard, 2005) is used. Since the analytical model (1) is subtidal, the viscosity profiles obtained from the GOTM are tidally averaged. These subtidal A_v profiles are analyzed using a peak-detection algorithm to capture the local maxima (i.e., prominent curvature changes near the surface and bottom, and around the mid-depth) and the associated values of A_v at these peaks. These subtidal A_v

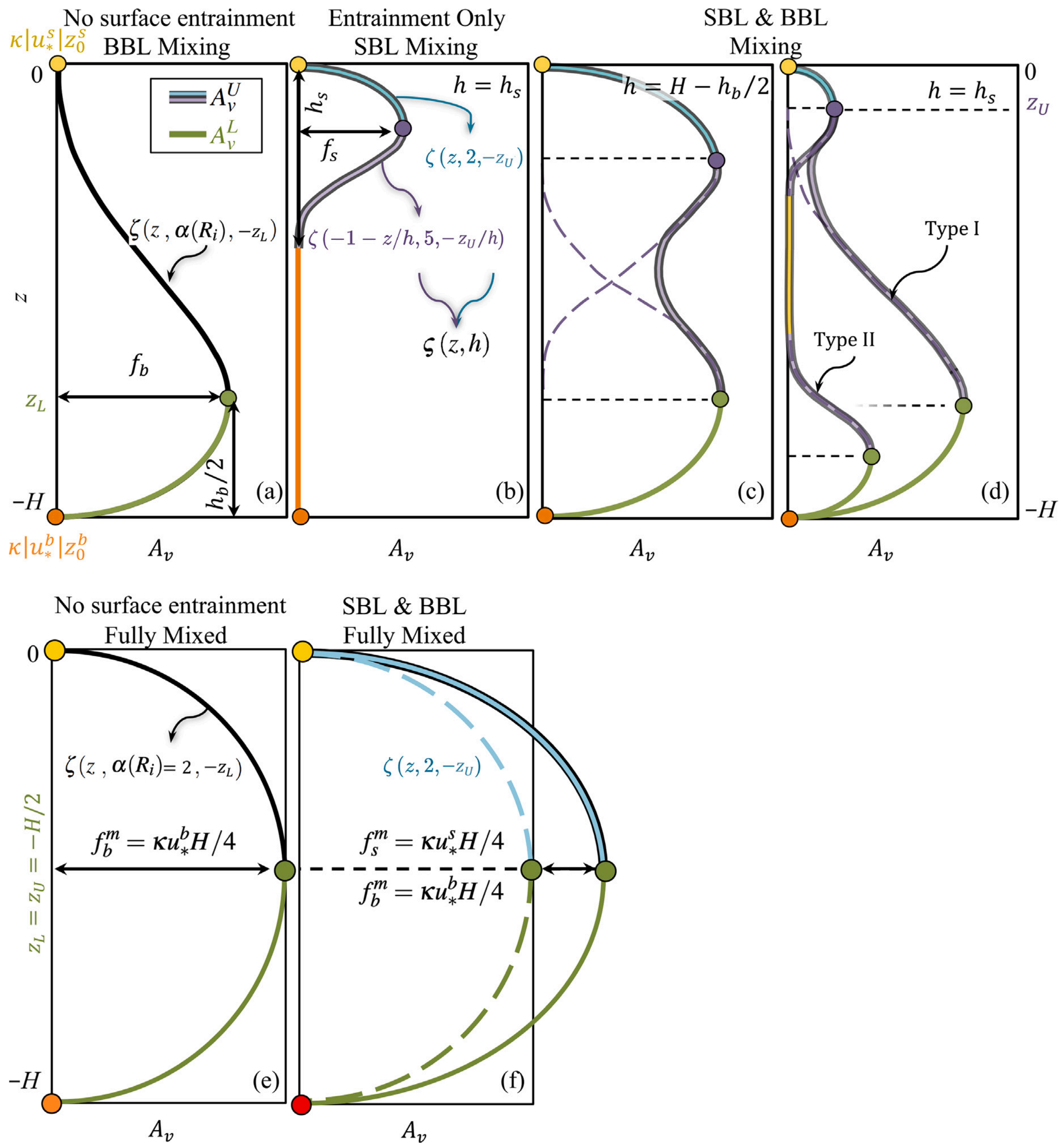

Fig. 1. A sketch of tidally averaged eddy viscosity A_v profiles resulting from Eq. (6) under stratified conditions: (a) only BBL mixing $h_s = 0$, (b) only SBL mixing $h_b = 0$, and (c, d) both BBL and SBL mixing when $\{-z_U, z_L - H\} < H/2$. Critical depths with boundary conditions are marked by circles e.g.,yellow/orange circles are associated with A_v at surface/bottom. The shape functions ζ, ς are shown in color to specify their associated layer (Appendix A). The length scale h−associated with SBL mixing, is shown on the top right corner. It indicates the depth where the upper layer A_v^U maximum decays and merge onto the layer below. A Type II profile denotes the conditions of $h_s + h_b < H$. The $A_v(-h)$ equals: (b) $\kappa|u_*^b|z_0^b$ without BBL mixing, (d) $\kappa|u_*^s|z_0^s$ with BBL mixing. A Type I profile (c, d) denotes the surface entrained conditions with $h_s + h_b > H$. The A_v profile is parabolic when $z_U = z_L = -H/2$. (e, f) Fully mixed conditions without and with surface entrainment. Red circle in (f) denotes $\kappa(|u_*^s| + |u_*^b|)z_0^b/2$ in case of $d_0 > 0$ (solid line). Green line denotes the BBL; black line denotes the upper layer without SBL; blue and purple lines denote the A_v^S and A_v^I, respectively.

characteristics are systematically investigated over the space of W, S_i and U_n; via scaled potential energy anomaly, R_i and S_i are interlinked (Appendix B); the boundary layer thicknesses h_s and h_b are expressed in terms of the state parameters and the local maxima positions z_U and z_L are linked to them (Appendix C, Fig. Ca, b).

This systematic investigation is performed by considering a set of idealized case studies in which the tidal current amplitude U_T (M_2 with T = 12.42 h), wind stress τ^s, and longitudinal salinity gradient $\partial_x S (= -g\beta\partial_x b$ with haline contraction coefficient $\beta = 7.4 \times 10^{-4}$ kg g^{-1}) are systematically varied, while the other parameters are fixed: $H = 10$ m, $z_0^b = 3 \times 10^{-3}$ m, $z_0^s = 1.5 \times 10^{-5}$ m, and zero runoff velocity $u_r = 0$ m s^{-1}. The number of GOTM experiments carried out is around 12,000. From the GOTM runs that reach a periodic state, u_*^b is obtained after tidally averaging the GOTM output, resulting in the dimensionless state parameters with ranges $U_n \in [0.01, 1.4]$, $W \in [-2.3, 2.3] \backslash \{0\}$, and $S_i \in [0.02, 1.60]$.

3.1. Calibration of A_v

The GOTM simulations are grouped into weak, moderate, and strong tidal forcing, respectively indicated by $U_n \sim \mathcal{O}(1)$, $U_n \sim \mathcal{O}(10^{-1})$, and $U_n \sim \mathcal{O}(10^{-2})$ (Fig. 2 left, middle and right columns). For a fully-mixed water column, i.e., $f(R_i = 0) = 1$, unsteadiness magnitudes of $U_n = 1$ $U_n = 0.1$ and $U_n = 0.01$ correspond to tidal velocity amplitudes of

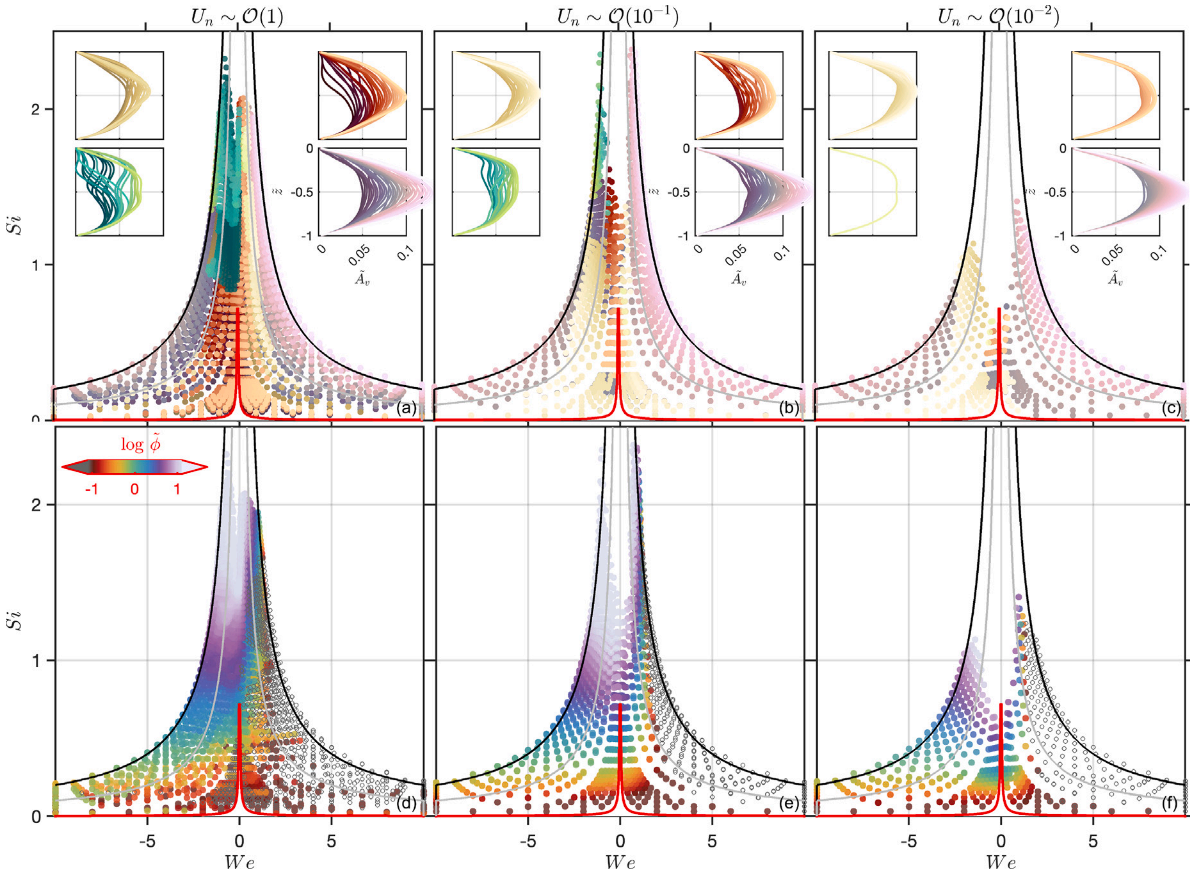

Fig. 2. Tidally averaged and scaled eddy viscosity $\tilde{A}_v = A_v/(u_*^b H)$ profile characteristics: (a–c) profile shape, and (d–f) scaled potential energy anomaly $\tilde{\phi}$ (< 0 for unstably stratified conditions shown in gray circles) derived from GOTM. (a–c) The simulations are grouped in three orders of magnitudes of the unsteadiness numbers $U_n \sim \mathcal{O}(1), \mathcal{O}(10^{-1}), \mathcal{O}(10^{-2})$ with panel-columns denoting the increasing tidal amplitudes from left to right. The simulations are shown over the parameter space of the Wedderburn and the Simpson numbers $We - Si$; the scaled wind stress $|W| = 0.01$, $|W| = 1$, and $|W| = 2$ are drawn in red, gray and black contours. In top panel, colors denote the local maximum of each tidally averaged $\tilde{A}_v$ within each profile cluster; all $\tilde{A}_v$ profiles are grouped based on their shape (inset figures) i.e.,local maximum is at the mid–depth (pink/brownish), near the surface (yellow), near the bottom (red), or bimodal (green) with lighter shades denoting larger magnitudes. The GOTM runs that did not reach a periodic state are blanked out. $We > 0$ indicates up-estuarine winds and $We < 0$ indicates down-estuarine winds.

0.03, 0.25, 2.5 m s^{-1} using the default parameter values. The tidal amplitudes obtained from (3) have to be multiplied by $f(R_i = 5) = 1.77$ for fully-stratified conditions under relatively weak winds; the upper limit choice for the bulk stratification $R_i = 5$ is detailed in Fig. 3a of Basdurak et al. (2021). Fig. 2 reveals the complex dependence of the A_v-profile on stratification (in both horizontal and vertical directions), directional (up- and down-estuarine) wind−intensity, and tidal forcing characteristics. In Fig. 2a–c, characteristics of the tidally-averaged and scaled (by $u_*^b H$) GOTM−A_v profiles are plotted as a function of W_e (horizontal axis) and S_i (vertical axis) with colors indicating the overall shape of each profile and color-shades denoting the relative local-maxima intensity. The shape of the A_v profiles ranges from skewed, with distinguished BBL-peak (red) or SBL-peak (yellow), to twin-SBL-BBL-peaks (green) to parabolic (pink/brownish). These shapes resemble the 2-layer and 3-layer A_v profiles illustrated in Fig. 1, and will be captured by the associated A_v-parameterization (6). In Fig. 2d–f, the degree of vertical stratification corresponding to each profile is shown as the scaled (by $\rho_0 (u_*^b)^2$) potential energy anomaly. Contours of scaled wind stress $|W| (= 0.05, 1, 2)$ are shown in the panels of Fig. 2 to identify the regions of dominant stress. For decreasing U_n, the region that GOTM can resolve gets smaller (i.e., markers are constrained to a smaller region corresponding to smaller S_i).

Wind direction (W_e) and tidal strength (U_n) affect the position of the local maxima: weak tides and down-estuarine winds support the near-bottom skew (Fig. 2a) whereas strong tides and down-estuarine winds result in the near-surface skew (Fig. 2c). With increasing horizontal stratification S_i, twin-peak A_v shapes emerge for down-estuarine winds (Fig. 2a, b); the two peaks converge with increasing $|W|$ (left-bottom inset of Fig. 2a–b, lighter shades of green) approaching a parabolic profile. Focusing on the parabolic A_v profiles, it is observed that their magnitude linearly increases with $|W|$ independent of U_n (lighter shades of pink; Fig. 2a–c). However, for all cases, there is an asymmetry in local-maxima magnitudes in regard to the $W_e = W/S_i$. Such asymmetry is a result of differences in the degree of vertical stratification $\tilde{\phi}$. This is best observed in Fig. 2d–e in which vertical stratification increases as up-estuarine winds weaken and down-estuarine winds take over. Vertical stratification increases with horizontal stratification when winds are in the down-estuarine direction; under up-estuarine winds vertical stratification is more sensitive to the combined effect of the scaled wind stress W and S_i.

Additionally, increasing up-estuarine winds yield unstable conditions $\tilde{\phi} < 0$ (empty circles in Fig. 2d–e). This region of the parameter space coincides with A_v profiles of scaled magnitudes $\tilde{A}_v > 0.1$, which can be attributed to the dominant effect of wind on the vertical stratification of the water column; hence the A_v profile scales with surface friction velocity rather than bottom friction velocity.

3.1.1. Surface boundary layer

The evolution of the SBL was first experimentally investigated by Kato and Phillips (1969). Based on these lab experiments, Price (1979) derived an entrainment law from energy conservation considerations, resulting in an expression for the SBL thickness given by

$$h_s(t) = \psi |u_*^s| \sqrt{\frac{t}{N_0}}. \tag{8}$$

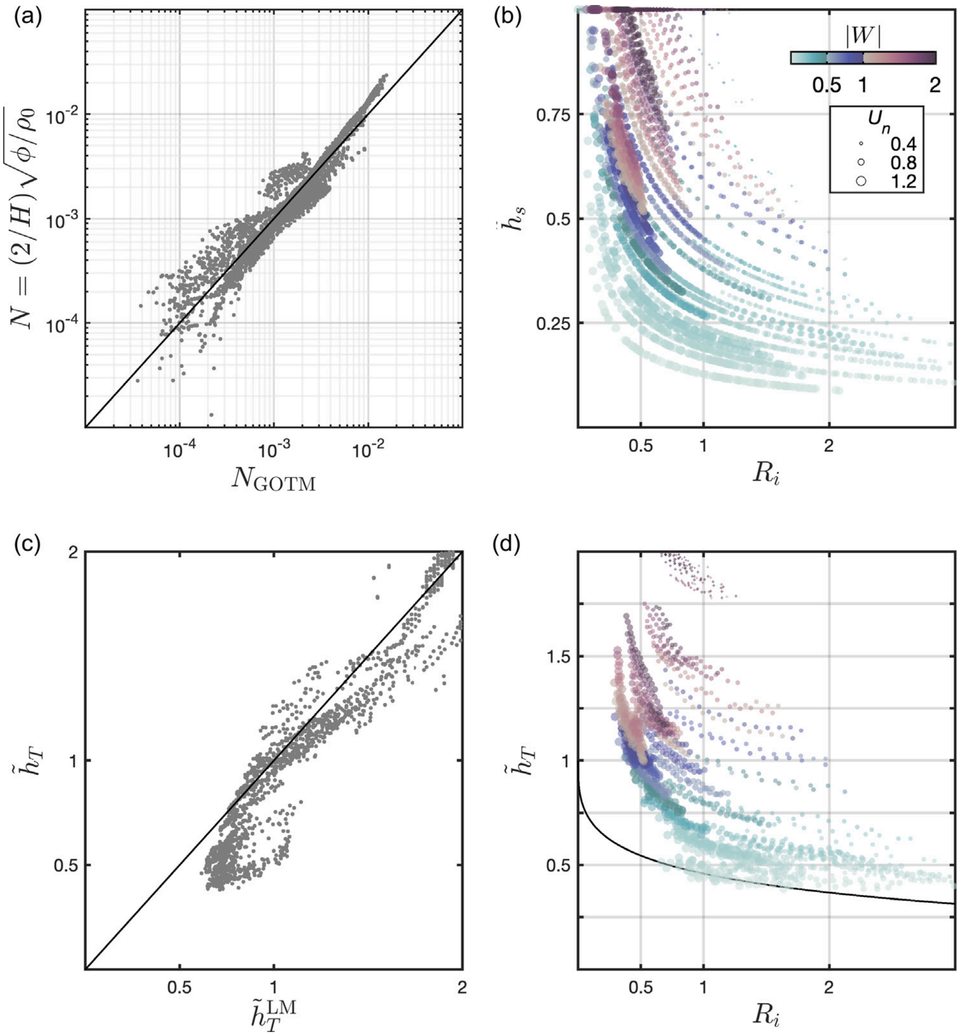

Fig. 3. (a) Bulk buoyancy frequency approximation N vs. N_{GOTM} for the SBL. (b) Tidally−averaged SBL thickness h_s as a function of vertical stratification R_i. (c) Comparison of $\tilde{h}_T$ and $\tilde{h}_T^{\mathrm{LM}}$, the sum of tidally−averaged and scaled boundary layer thicknesses $\tilde{h}_b = 2 + 2\tilde{z}_L$ and $\tilde{h}_s$ obtained by Eq. (10) and the tidally−averaged A_v-peak locations of with the superscript LM standing for 'Local Maximum'. (d) $\tilde{h}_T$ as a function of R_i with the black line drawn as a reference for no-entrainment case i.e., $\tilde{h}_T = \tilde{h}_b = \exp(r_1 R_i^{r_2})$ for stable conditions. For unstable conditions $\tilde{h}_s = \tilde{h}_b = H/2$. All the relations shown in (a–d) are based on the GOTM output with colors denoting the scaled wind stress magnitude $|W|$ (grouped in intervals of 0.5, 1 and 2), and circle-sizes denoting the unsteadiness U_n (smaller circles and U_n denoting larger tidal amplitudes).

In (8), t is time, N_0 is the Brunt Väisälä frequency prior to a wind event and $\psi \approx 1.1$ is a coefficient. Chen and Sanford (2009) adopted (8) to obtain a subtidal boundary layer thickness using a characteristic time scale for t = 3h, and for N_0 the constant background stratification, specific to their numerical model findings. We propose a more general approach for the subtidal SBL thickness based on a typical time scale defined as the quarter tidal period $t = T/4$, and the bulk buoyancy frequency N. Constraining $\tilde{h}_s$ by the water column depth (i.e., $h_s \leq H$) yields

$$h_s = \left[\psi |u_*^s| \sqrt{\frac{T}{4N}},\ H\right]_{\min}, \tag{9a}$$

$$N = \frac{2}{H}\sqrt{\frac{\phi}{\rho_0}}. \tag{9b}$$

For stable conditions ($R_f > 0,\ \ \phi > 0$), the approximation of N (9b) is compared with the tidally-averaged buoyancy frequency, resulting in N_{GOTM} obtained from the GOTM runs in Fig. 3a. The N_{GOTM} is calculated by first depth-averaging the buoyancy frequency $(1/z_j)\int_{z_j}^{0} N(z)\,\mathrm{d}z$, with z_j denoting the position of the maximum vertical density gradient (i.e., $\partial_z\rho|_{z=z_j} = (\partial_z\rho)_{\max}$ in the water column), then tidally averaging it. The lower integration limit is taken equal to z_j over z_U because it helps capturing the whole SBL not just the upper part of the SBL. The N_{GOTM} compares well to the N (9b).

The change of the SBL thickness h_s (9a) with $R_i(W, \tilde{\phi})$ is shown in Fig. 3b; h_s decreases with increasing stratification R_i and increases with scaled wind stress W. It is also sensitive to U_n: for a water column that has the same bulk stratification, cases with smaller U_n (higher tidal amplitudes and BBL mixing; shown as smaller markers in Fig. 3b) yield larger SBL layers, and vice-versa. The new subtidal SBL expression (9) is valid for stable conditions ($R_f > 0,\ \phi > 0$). For unstable conditions ($R_f < 0,\ \ \phi < 0$), it is considered to be equal to the water depth, $h_s = H$. This is driven by the GOTM output shown in Fig. 2 which suggests that the boundary layer thickness scales with the water depth for unstable conditions, yielding parabolic A_v shapes. Motivated by the findings of Trowbridge (1992) for stably stratified conditions, z_U is set to a water depth that separates the regions of distinct turbulent-mixing characteristics: the wall region where boundary-generated turbulence dominates mixing and the marginal-state region where turbulent mixing is strong enough to maintain the stratification near a critical value. A new relation for z_U and h_s that accounts for the merging boundary layers is derived and detailed along with the vertical structure of the SBL in Appendix A.3.

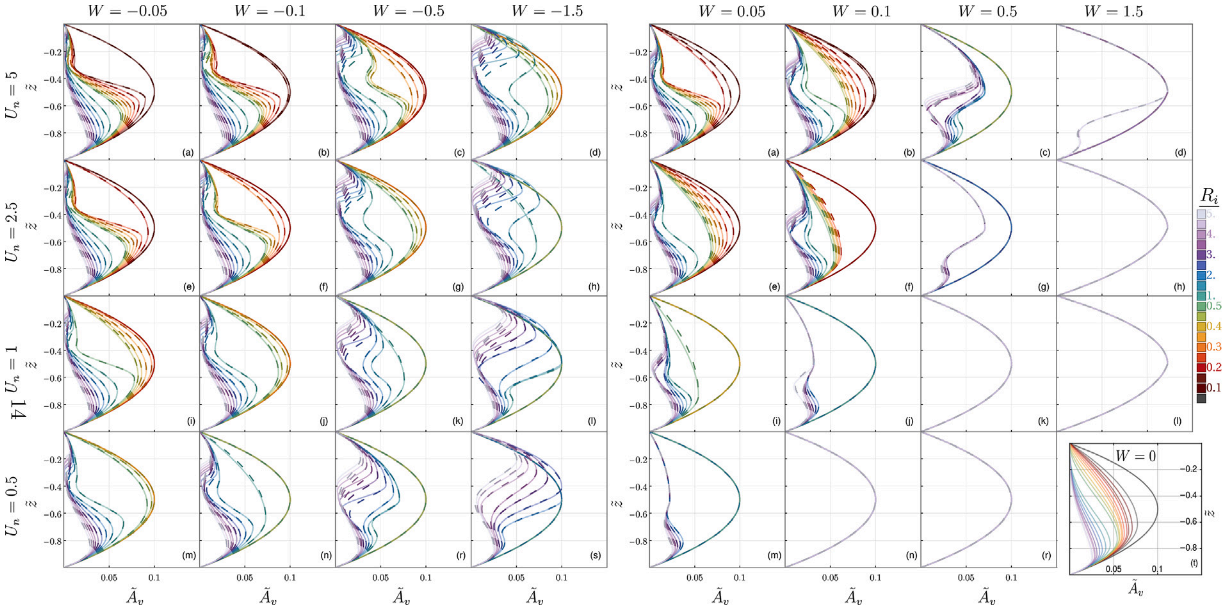

Fig. 4. Sensitivity of the $\tilde{A}_v$ parameterization to $|W|$ (columns), U_n (rows) and R_i (transparent colors) for down-estuarine (a–s; left panel) and up-estuarine winds (a–r; right panel); (t) a reference scenario when the surface entrainment is ignored (Basdurak et al. 2021). On the right panel (s) is excluded for simplicity as it is same as (l; right panel). Solid lines denote the parameterization and dashed lines denote the polynomial approximation. The profiles are ordered w.r.t. the degree of stratification with weaker stratification shown underneath. Hence, for a fully mixed water column with parabolic $\tilde{A}_v$, fewer lines are visible due to overlapping.

3.1.2. Bottom boundary layer

Wind entrainment changes the interfacial shear and the stratification of the water column. For shallow systems, dynamics of the SBL may affect the BBL characteristics. Therefore, the BBL-thickness formulation introduced by Chen and De Swart (2016) h_b^0 is extended to account for wind entrainment. This new formulation is obtained by first parameterizing the sum of tidally−averaged surface and bottom boundary layer thicknesses, $h_T = h_s + h_b$ in terms of W, S_i, U_n, and h_b^0, as:

$$h_T = \frac{h_b^0}{1 - 0.75 \tanh \sqrt{|W|/(S_i U_n)}}, \text{with } h_b^0 = H \exp(-0.78 {R_i}^{0.36}). \tag{10a}$$

This parameterization is obtained using the GOTM output. The sum of boundary layer thicknesses h_T varies between h_b^0 for the no-wind $W = 0$ cases and $\sim 4h_b^0$ for the cases of $|W| \gg S_i U_n$. The BBL thickness h_b is then calculated by using (9) and (10a), resulting in

$$h_b = \begin{cases} H, & h_s = H. \\ (h_b^0, H)_{\min}, & h_t \leq h_s < H. \\ (h_T - h_s, H)_{\min}, & h_t > h_s < H. \end{cases} \tag{10b}$$

Note that the upper limit is constrained by the water column depth i.e., $h_b \leq H$; accordingly, $h_t \leq 2H$ because a fully mixed water column may arise due to the growth of SBL or/and BBL. When the wind entrainment is insignificant e.g., $W_e = W = h_s = 0$, then h_T reduces to h_b^0 in agreement with Chen and De Swart (2016) and Basdurak et al. (2021).

The correlation between the total boundary layer thicknesses obtained using the GOTM output h_T^{LM} and h_T (10a) is shown in Fig. 3c. The h_T^{LM} is calculated by detecting the tidally-averaged A_v-peak locations (i.e., the local maxima z_U and z_L) and relating them to the surface and bottom boundary layer thicknesses h_s^{LM} and h_b^{LM}. The former is achieved by using (A.3) and the latter by assuming $h_b^{\mathrm{LM}} = 2(z_L + H)$ (consistent with Basdurak et al. (2021)). The sum of boundary layer thicknesses resulting from both methods are in good agreement, indicating that (10) offers a reasonable estimate for the total boundary layer thickness for stable conditions. With increasing wind adjusted vertical stratification R_i the sum of the boundary layer thicknesses h_T decrease; when the scaled winds ($|W|$) weaken, the exponential trend associated with the BBL alone is captured (black line in Fig. 3d). For unstable conditions, analogous to the SBL, the BBL thickness scales with the water depth.

3.2. Sensitivity of the A_v-parameterization to R_i, W and U_n

With boundary layer thickness definitions and the associated local-maxima relations, expressed in terms of the state parameters, (6) results in physically motivated, tidally-averaged A_v profiles. Because the prominent subtidal characteristics of the A_v profiles (i.e, z_U, z_L, f_s, and f_b) in (6) are based on the GOTM output and thus already qualitatively validated, an explicit comparison between them is excluded for simplicity.

In Fig. 4, the A_v profiles are shown for a range of dimensionless parameters: $R_i = [0.05, 0.1, \ldots, 0.5, 1, \ldots, 5]$, $|W| \in \{0.05, 0.1, 0.5, 1.5\}$, and $U_n \in \{0.5, 1, 2.5, 5\}$. For smaller values of unsteadiness i.e. $U_n \sim \mathcal{O}(10^{-2})$, the BBL mixing increases resulting in parabolic profiles. Therefore, we focus on the part of the parameter space with a wider range of A_v profile variability.

An important consequence of the surface-entrainment inclusion is that the vertical gradient of the A_v profile increases near the surface similar to its linear increase near the bed regardless of stratification, resulting in a parabolic A_v profile near both boundaries (Fig. 4a–s, left and right panels). When surface entrainment is neglected, the parabolic profile near the surface is missing for stratified water column (Fig. 4t).

The profile shape is more sensitive to stratification under down-estuarine winds (Fig. 4, left panel) than under up-estuarine winds (Fig. 4, right panel); its local maximum shifts between near-bed and near-surface. In contrast, up-estuarine surface forcing yields mostly parabolic eddy viscosity profiles for any degree of stratification except for large U_n and small W. When tidal velocity amplitudes and down-estuarine winds are weak (larger U_n and smaller W; Fig. 4a left panel), the A_v-local maximum occurs near the bed. The A_v-local maximum occurs near the surface for smaller U_n and larger W (Fig. 4s left panel). In between these extremes, relative magnitudes and locations of the A_v-maxima vary. When U_n is relatively big and the bottom stress is greater than the wind stress $|W| < 1$, the BBL grows with increasing winds more than the SBL due to wind-adjusted bottom stress (Fig. 4a–c left panel). For $|W| > 1$ the SBL growth dominates the stratified water column ($R_i > 1$) reducing the BBL height (Fig. 4d left panel). Up-estuarine winds yield parabolic profiles, mostly associated with a well-mixed water column with increasing W and decreasing U_n. This is the case even for a relatively strong stratified case $R_i > 1$ (Fig. 4a–d vs. Fig. 4m–s). Up-estuarine winds reduce the BBL height and lead to wind induced high eddy viscosity coefficients with parabolic profile under relatively strong stratification (right panel of Fig. 4). Most of $W > 0.5$ is associated with unstable stratification and hence strong mixing.

3.3. Sensitivity of h_s and h_b to S_i, W and U_n

The surface and bottom boundary layer thicknesses are explored over the state parameters (Fig. 5). The parameter space is spanned by U_n, W and S_i rather than R_i to be consistent with Part I (Basdurak et al., 2021). In Fig. 5, each boundary layer thickness is shown by a distinct color with top half of the markers denoting the SBL and the bottom half denoting the BBL. Markers without black circles indicate separate layers (Fig. 1d:Type II), whereas merging boundary layers (Fig. 1c, d:Type I, f) are shown with black circles. The boundary layers separate as the horizontal stratification increases (S_i gets bigger) when $W < 0.5$ and $U_n = 5$ (Fig. 5a). The bottom boundary layer thickness h_b is greater than h_s for down-estuarine winds and vice versa for the up-estuarine winds. Increasing tidal strength constrains the occurrence of separate layers to weaker down-estuarine winds (Fig. 5d). When either of the boundary layers scales with the water depth (purple markers), the A_v profiles become parabolic.

4. Exchange flow

4.1. Analytical solution

The analytical solution for tidally averaged exchange flow is given in Part I (Eqn. (16) of Basdurak et al. 2021) and expressed in its scaled form as:

$$\tilde{u}(\tilde{z}) = \tilde{U}_g + \tilde{U}_w + \tilde{U}_r = \frac{S_i}{2}\gamma_g + W\gamma_w + \tilde{u}_r\gamma_r \,. \tag{11}$$

Here, $\tilde{U}_g$, $\tilde{U}_w$, and $\tilde{U}_r$ denote the density-driven, wind-driven and runoff flow components, respectively; γ_j is a shape function associated with each component with $j \in \{g, w, r\}$, dependent on the shape of the A_v profile (Eq. (5)). Note that the notations for scaled wind stress and Wedderburn numbers are different in Part I.

Here, we follow the same procedure as in Part I, and use the constrained-polynomial fitting for the upper layer of the A_v within $z_L \le z \le 0$ to avoid Fractional Calculus problems in solving $\tilde{u}$. The main difference with Part I is that the A_v^U approximations and thus γ_j in (11) can be single or two-layered (Appendix C). The fitted A_v profiles are shown in Fig. 4 as dashed lines. The approximation agrees well with the A_v parameterization except when the mid-layer A_v is orders of magnitude smaller compared to the rest of the water column (Type II in Fig. 1d; pronounced when $R_i \ge 3, U_n \ge 2.5$ and $W < 0$ in Fig. 4). For these extreme cases, exponential approximation for the mid-layer (interfacial layer) yields better results (Fig. D1, bottom-right panel; Appendix D.1). However, we use polynomial approximation as these cases are rare in the parameter space explored and computationally costly. Note that because the lower layer A_v^L is parabolic, the analytical solution does not require using the approximation. The local maxima positions and magnitudes, and the surface magnitude of the approximated A_v profiles are same as in (6) i.e., continuous in depth satisfying the boundary conditions. With these profiles, the tidally averaged flow components are solved analytically. Exchange flow velocity is explored over a range of state parameters in the following section.

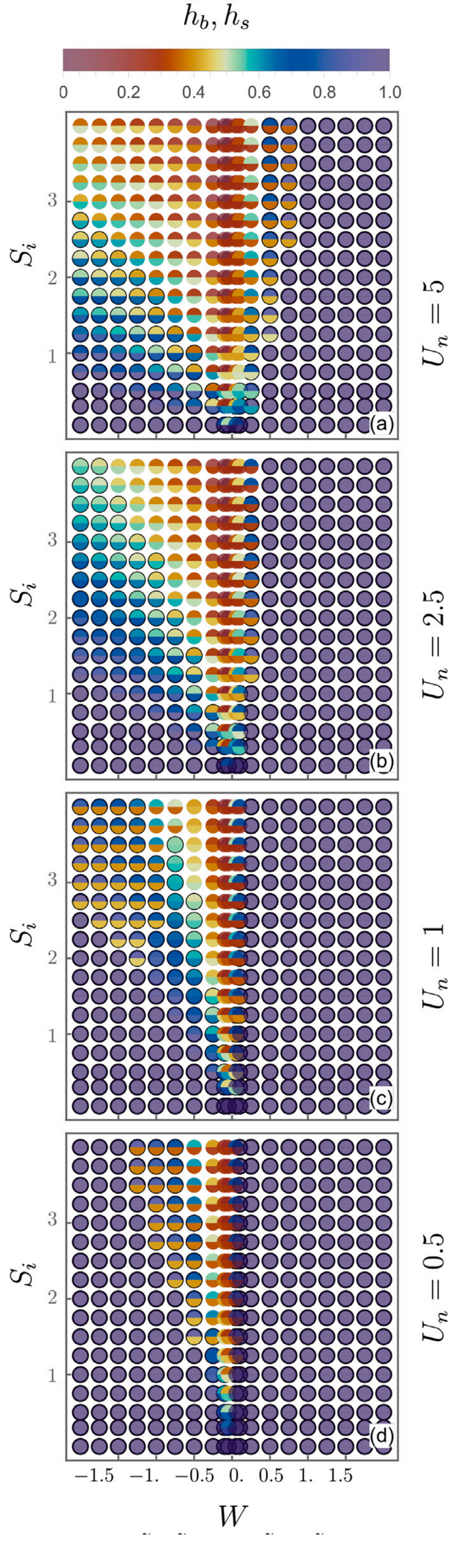

Fig. 5. Scaled boundary layer thicknesses $\tilde{h}_b, \tilde{h}_s$ with $\tilde{h}_s + \tilde{h}_b \ge 1$ shown in black circles. Bi-colored markers are used for boundary layer thicknesses with top and bottom halves denoting $\tilde{h}_s$ and $\tilde{h}_b$.

4.2. Exchange flow profiles

Scaled exchange flow $\tilde{u}$ profiles that are obtained from analytical solutions using (6) of the depth-varying A_v (dashed lines, Fig. 4) are shown in Fig. 6 for no-runoff condition $\tilde{u}_r = 0$. By using (3), one can

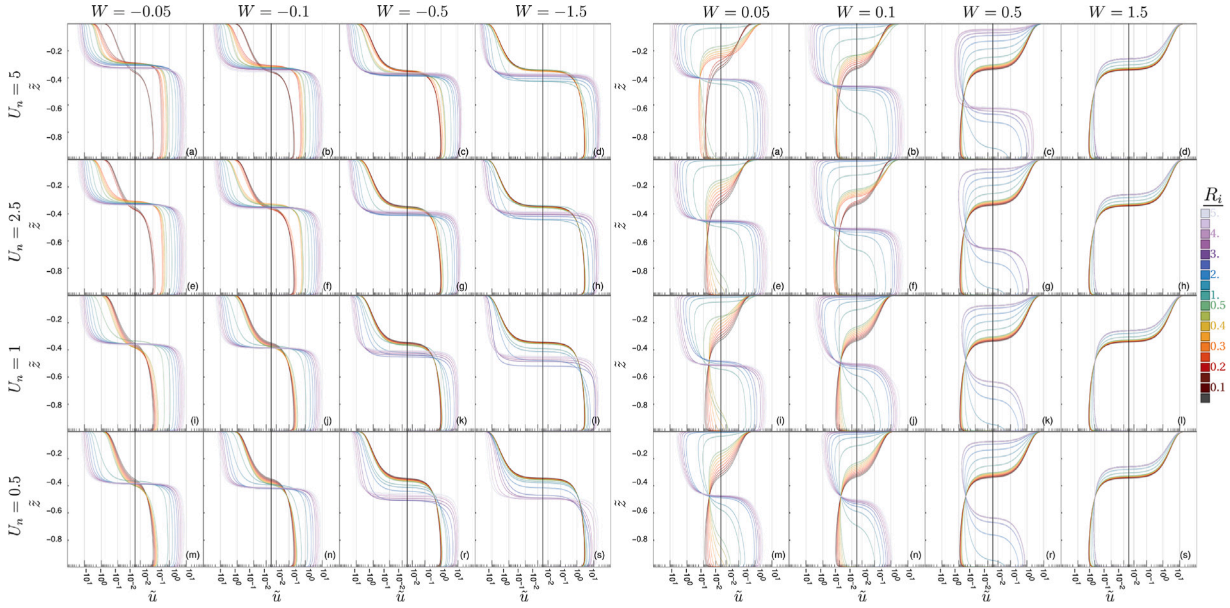

Fig. 6. Sensitivity of the exchange flow $\tilde{u} = \tilde{u}_g + \tilde{u}_w$ to $|W|$ (columns), U_n (rows) and R_i (transparent colors) for down-estuarine (a–s; left panel) and up-estuarine winds (a–s; right panel). The profiles are obtained analytically using the polynomial-approximated $\tilde{A}_v$-parameterization (dashed lines in Fig. 4). Note that the currents are shown on a logarithmic scale for a better visualization and that all the flow profiles converge to zero at the bottom of the water column.

recover the dimensional form of the exchange flow u. The $\tilde{u}$ profiles vary in shape and magnitude over the parameter space of $|W|$, U_n and R_i. Shape of the exchange profiles are characterized by their inflection depths that correspond to changes in flow's direction yielding multi-layer flow. Down-estuarine winds drive two-layer flows (Fig. 5, left panel) whereas up-estuarine winds drive two and three-layer flows (Fig. 5, right panel). Down-estuarine winds support the classical estuarine circulation with downwind estuarine flow near the surface and upwind return flow near the bottom. Down-estuarine winds yield enhanced exchange flows with increasing stratification. With increasing down-estuarine wind stress, stronger stratification cause the inflection depth to move down approaching the mid-water column. There is a distinct grouping of $\tilde{u}$ profiles for $R_i > 1$ and $R_i < 1$ due to the interplay between stratification and shear; $R_i = 1$ separates stratified conditions from mixed conditions, $R_i < 0.1$ denotes the fully-mixed conditions. For weaker down-estuarine winds, the inflection depth varies with tidal amplitude rather than stratification (Fig. 5a, e, i, m; left panel), increasing with tidal amplitude. For stronger down-estuarine winds, the inflection depth varies with both tidal amplitude and stratification (Fig. 5d, h, l, s; left panel). For up-estuarine winds, $\tilde{u}$ reversals (inverse circulation: up/down-estuarine flow near the surface/bottom) or three-layer flows occur (i.e., mid-depth upwind flows balanced by downwind flows near the top and bottom of the water column). Inverse circulation occurs when $W = 1.5$ (Fig. 5d, h, l, s; right panel) and relatively weakly stratified conditions of $W < 1.5$. The three-layered $\tilde{u}$ form is more prominent when $W = 0.5$ and $R_i > 1$ (Fig. 5c, g, k, r; right panel). For weak winds and stratified waters (first two columns of Fig. 5 right panel) the down-wind flow gets constrained to the surface. For $W > 1$, $\tilde{u}$ is less sensitive to stratification as the unstable conditions prevail for any R_i range. This yields two-layer flows with near surface inflection (in contrast to the near-bottom inflection of down-estuarine winds).

5. Exploration of the exchange flow characteristics

The exchange flow intensity $\tilde{M}$ (Burchard et al., 2011) for one-dimensional cases, defined as

$$\tilde{M} = 4\int_{-1}^{0} \tilde{u}(\tilde{z})\,(\tilde{z}+0.5)\,d\tilde{z} \tag{12}$$

is used to explore the state space spanned by the parameters of U_n, W and S_i rather than R_i to be consistent with Part I (Fig. 7c in Basdurak et al. (2021) with x-axes denoting the scaled wind stress i.e., a different notation was used for the Wedderburn number).

The dimensionless exchange intensity $\tilde{M}$ considers the orientation of the near-bed currents and denotes classical (inverse) circulation when $\tilde{M} < 0\,(\tilde{M} > 0)$. The exchange flow intensity in (12) differs from the definition used in Part I where it was modified to include the BBL thickness; the original form is used here to accommodate for the merging boundary layers.

The exchange flow intensity in Fig. 7 g differs from the ones shown in Part I that ignore wind entrainment. Ignoring wind entrainment results in two orders of magnitude difference in $\tilde{M}$ for the cases of extreme stratification $S_i > 3.5$ (whited area in Fig. 7c, of Part I where $U_n = 0.03$; the whited area extended to $S_i > 1$ for $U_n = 0.5$ (not shown)). The $\tilde{M}$-isolines show asymmetry with respect to wind direction and stratification (Fig. 7, left panel). The exchange flow intensity $\tilde{M}$ increases with increasing up-estuarine winds and decreasing stratification; however it only increases with increasing down-estuarine winds and increasing stratification for $S_i <\sim 1$. For larger S_i the isoline slope first becomes negative ($\tilde{M}$ increases with weak down-estuarine winds) then positive with increasing down-estuarine winds. For weak tides, negative isoline slopes extend a wider span of $W - S_i$ space (Fig. 7a, darker shades of purple); for water columns with same stratification weaker down-estuarine winds result in stronger exchange. For weak tides and extreme stratification $S_i > 3.5$, $\tilde{M}$ becomes less sensitive to the down-estuarine wind stresses (Fig. 7a). Additionally, moderate to strong up-estuarine winds that are mostly associated with unstable stratification, yield approximately half the exchange-intensity of the down-estuarine winds with same strength.

The down-estuarine wind driven reversals of $\tilde{M}$-isolines (darker shades of purple in Fig. 7, left panel) correlate to the cases of $h_s + h_b < H$ (Fig. 5). These are the cases of A_v profiles with separate near surface and near bottom maxima. Variability of the SBL to BBL thickness increase with U_n (Fig. 5). The smaller the boundary layer thicknesses, the stronger the exchange intensity (Fig. 5; Fig. 7, left panel). When both SBL and BBL scale with H (dark-purple filled circles associated with parabolic eddy profiles), $\tilde{M}$-isolines slopes tilt in the same direction (positive slope) regardless of the wind direction. Markers denoting the boundary layer thicknesses that are $h_s + h_b \geq H$, yet individually smaller than the water depth (bi-color-filled black circles) correspond to the area of transition in trends of $\tilde{M}$-isoline slopes.

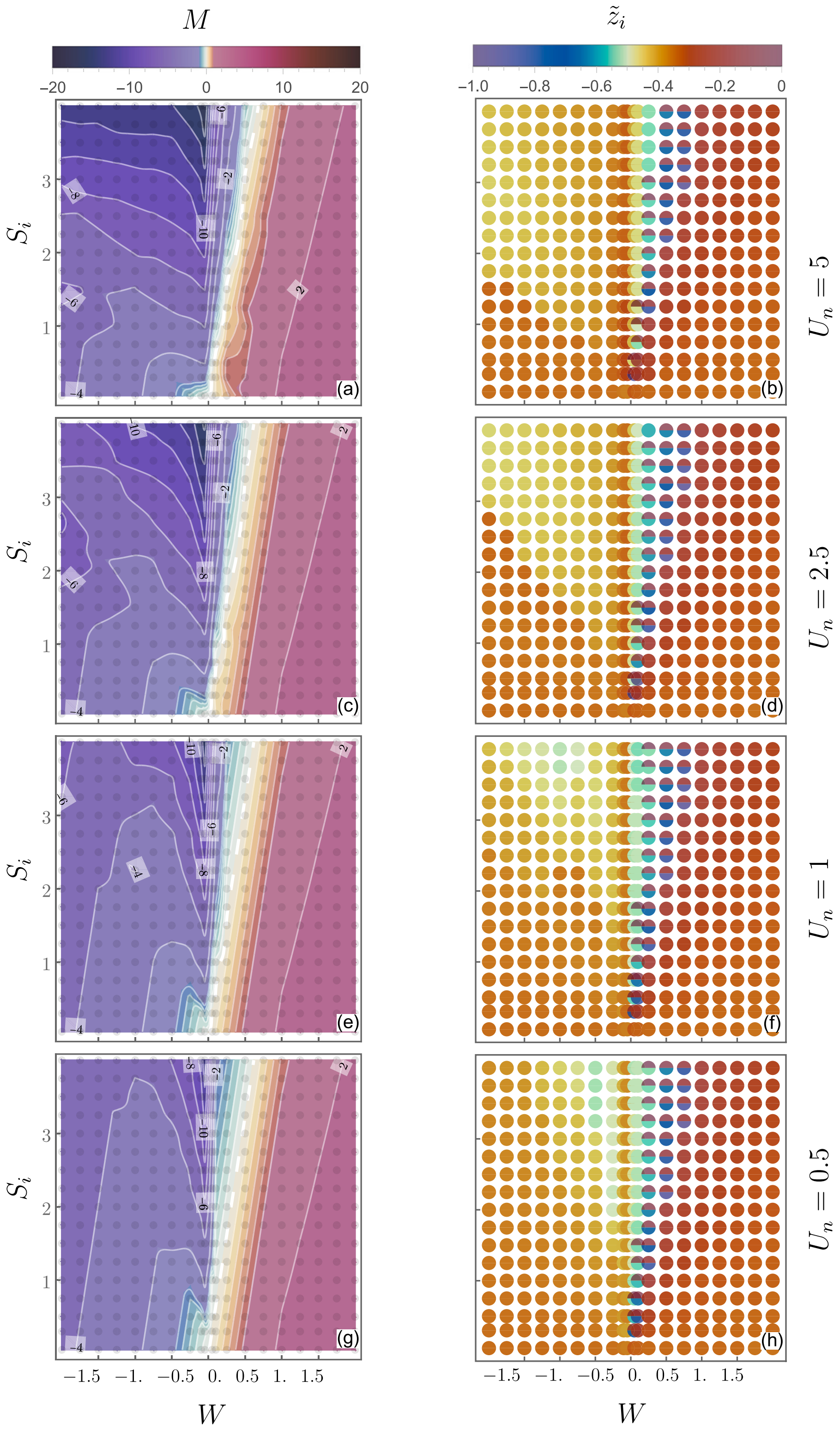

Fig. 7. Scaled exchange flow intensity M (left; with $|M| \leq 1$ range shown in distinct colors) and scaled inflection depth $\tilde{z}_i$ (that corresponds to change in flow direction). Single filled color denotes single inflection depth; dual inflection is shown with bi-colored filled markers top/bottom half denoting the near surface/bottom inflection depth.

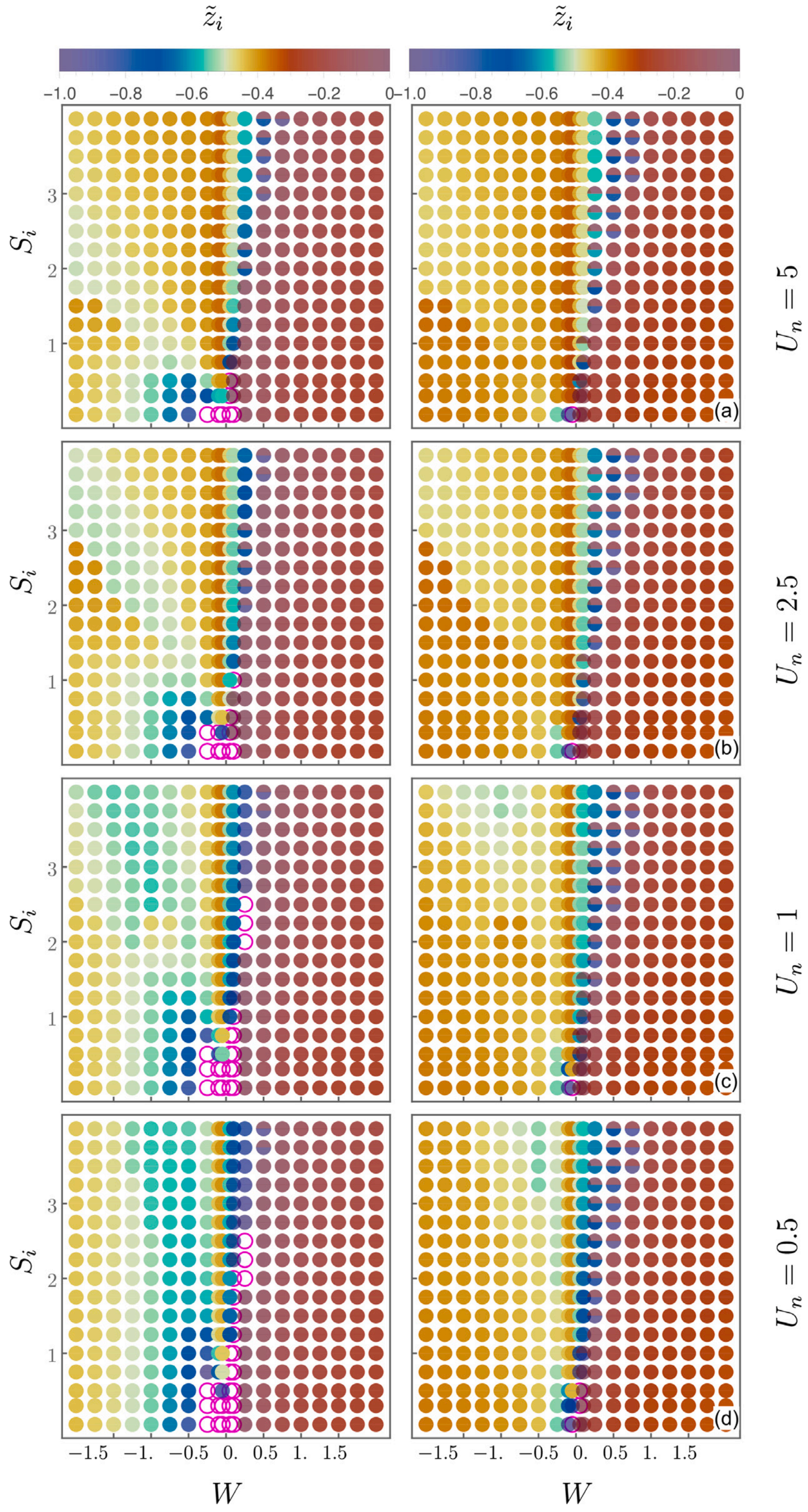

Fig. 8. Scaled inflection depths z_i, i.e., depths that correspond to changes in flow direction for $\tilde{u}_r = \{-1, -0.25, 0\}$ from left to right. Single filled color denotes single inflection depth; dual inflection is shown with bi-colored filled markers top/bottom half denoting the near surface/bottom inflection depth; single layer flows are shown in magenta circles.

5.1. Flow inflection depths and runoff

The $\tilde{u}$-structure changes across the parameter space are shown in terms of inflection depths $\tilde{z}_i$ that mark the changes in flow direction in the water column (Fig. 7, right panel; two and three layered flows are shown as filled markers, dual-filled markers, respectively). Mostly two-layer flows occur across the $W - S_i - U_n$ space with $-0.8 \geq \tilde{z}_i \geq -0.15$. The inflection occurs above mid-depths when both SBL and BBL scales with H.

With increasing down-estuarine runoff, the inflection depth shifts down/up for down/up-estuarine winds (Fig. 8). When $h_s + h_b < H$, the flow changes direction at mid-depth. Increasing down-estuarine runoff also supports the single-layer flow occurrences for weak-wind cases. Single layer flow (marked by magenta circles) is prone to U_n appearing only under relatively well-mixed conditions when U_n is significant. Flow becomes three-layered by the up-estuarine winds; favored by stronger stratification, but suppressed by down-estuarine runoff.

5.2. Modifications to $\tilde{u}$

As stated in Part I (Basdurak et al., 2021), the tidal variations in eddy viscosity profile are ignored in the analytical solution yielding underestimations in the exchange flow as a result of the absence of ESCO-generated circulation. To evaluate the accuracy of the exchange flow (8), the correlation of the exchange flow intensity between the numerical and analytical solutions is analyzed for the overlapping parameter space (Fig. 9). Same U_n range as in Fig. 6 is used for this analysis and the analytical solutions are obtained accordingly.

Analytical and numerical model results are in good agreement for relatively small unsteadiness numbers $U_n \sim 0.03$ (Fig. 9j). For weak tidal amplitudes, a decent agreement only exists for $R_i \sim 0.5$ when $|W| > 0.5$. The discrepancies arise with smaller $|W|$ for a varying degrees of stratification, particularly for down-estuarine cases (Fig. 9a, d, g). However, the comparison shows that the inclusion of wind-entrainment to the stratification adjustment and to the eddy viscosity parameterization improves the solution significantly for a wider range of state parameters (Fig. 9a, d, g of Basdurak et al., 2021).

To account for the ESCO-generated circulation, $\tilde{u}$ is modified by altering the contribution from the gravitational component and re-calculating M_{MODEL} (Fig. 9; middle and right panels). For $U_n \sim 0.03$ increasing the contribution from the gravitational component does not affect the correlation much. However, for higher unsteadiness numbers the correlation improves with $3\tilde{U_g}$ (Fig. 9c, f, i).

6. Comparison to observations

The tidally averaged A_v parameterization is compared to observations from the York River, a partially mixed estuary located around Chesapeake Bay, Virginia (Simpson et al., 2005). The estuary is forced by tidal currents and highly variable discharges. The survey was conducted at an almost straight section of the estuary, by using a combination of instruments (fast sampling ADCPs (Acoustic Doppler Current Profilers), an Acoustic Doppler Velocimeter (ADV), CTD profilers, and an anchored research vessel between ADCPs) capturing the neap-spring cycle of turbulence in the water column.

To compare the observed A_v profiles with those obtained using the parameterization developed in this paper, Figs. 2, 7, 8 of Simpson et al. (2005) were digitized by using image-processing techniques. The extracted images were re-constructed to correspond to the temporal resolution of the original images by using a lanczos filter for the time series at each depth with a relevant cutoff frequency (i.e., sampling frequency of the variables), yielding profiles of density, along-channel velocity, eddy viscosity and time series of bottom stress horizontal density gradient, bottom stress, wind speed and direction (Fig. 10). To calculate the state parameters, first the friction velocities $u_*^{b,s}(t)$ were computed (Fig. 10g, left axes). Winds were rotated 30 degrees west of north to conform to the main axis of the York River yielding along-channel wind speed $V(t)$ (< 0 down-estuary) and $u_*^s(t) = \sqrt{c_D^s \rho_{air}/\rho_0} V(t)$; $u_*^b(t) = \sqrt{\tau^b(t)/\rho_0}$. The state parameters $W(t)$ and $\tilde{\phi}(t)$ were calculated via scaling $u_*^s(t)|u_*^s(t)|$ and ϕ/ρ_0 by $u_*^b(t)^2$. The tidal R_i was obtained via (B.1) at the tidal scales with $W(t)$ and the scaled potential energy anomaly $\tilde{\phi}(t)$. Both $R_i(t)$ and $W(t)$ were then tidally averaged. For U_n the M2 period and absolute value of the tidally averaged bottom friction velocity were used.

The $A_v(t)$ was re-constructed by including its approximate magnitudes at the boundaries: $A_v(z = -H, t) = \kappa z_0^b u_*^b(t)$, $A_v(z = 0, t) = \kappa z_0^s |u_*^s(t)|$ with $z_0^b = 0.00005$ m and $z_0^s(t) = 1400(u_*^s(t))^2/g$. The boundary conditions were added to (Fig. 10b) and data gap was filled with 2D interpolation (Fig. 10c); the time series were scaled by $Hu_*^b(t)$ (Fig. 10d) and tidally-averaged. Tidally averaged A_v profiles under down-estuarine winds are shown in Fig. 10h.

During the neap tide, the wind direction is predominantly down-estuarine with strong winds, allowing for both SBL and BBL to develop. Due to relatively strong stratification, mid water column shows a smaller mixing coefficient setting the boundary layers apart (Fig. 10h, left axis). During spring tides, tidal mixing prevailed yielding mixed water column; the down-estuarine winds were relatively weak yielding a defined BBL with greater A_v magnitudes.

For the similar range of state parameters, the neap observations fall between Fig. 4n–r (purple line; left panel), and spring observations between Fig. 4m and Fig. 4t ($W = -0.05$ left panel and $W = 0$; green line). The parameterized profiles are in good agreement with the observed profiles. The parameterization does a decent job not only predicting the tidally averaged boundary layer characteristics, but also the A_v local maxima magnitudes.

7. Discussion

With the newly developed parameterization of A_v, the one-dimensional analytical solution provides insights into not only the composition of exchange flow profiles, but also its relation to the boundary layer properties over a wide range of state parameters i.e., stratification, unsteadiness and scaled wind stress.

For a fixed S_i, U_n, and $|W|$, down-estuarine winds result in tidally averaged exchange flows that have twice the amplitude of those caused by up-estuarine winds. Up-estuarine winds with magnitude $W >\sim 0.5$, are associated with unstable stratification. This unstable stratification is the result of extreme A_v coefficients during the tidal cycle; these intertidal signals strongly affect the tidally averaged A_v profiles. The exchange flow is reduced with increasing W. The exchange flow intensity $\tilde{M}$ is most sensitive in the range of $-0.5 \leq W \leq 0.5$. For strong unsteadiness numbers and strong stratification, increase in scaled down-estuarine wind-stress does not affect the exchange intensity $\tilde{M}$.

Additionally, SBL and BBL thicknesses affect the exchange flow structure and intensity. The exchange flow intensity trends over the $W - S_i$ space become nonlinear ($\tilde{M}$-isolines slanted in different directions) when $h_s + h_b < H$ associated mostly with down-estuarine winds.

The novel A_v parameterization can also be used in estimating tidally averaged eddy viscosity profiles in observational estuarine studies with a wide range of wind forcings when turbulent measurements are unavailable. One of the limitations of the model is that the tidal variations in eddy viscosity are excluded for simplicity. Therefore, the covariance of eddy viscosity with vertical shear and its effect on the exchange flow is not considered. This will be addressed in future research.

Furthermore, the novel A_v parameterization can be integrated in salinity models to better understand the relative importance of the wind-induced terms i.e., salinity shear, depth-averaged salinity gradient and vertical mixing at subtidal time scales. Using a constant eddy viscosity coefficient Jongbloed et al. (2022) found that the influence of extended periods of increased wind forcing may trigger a regime

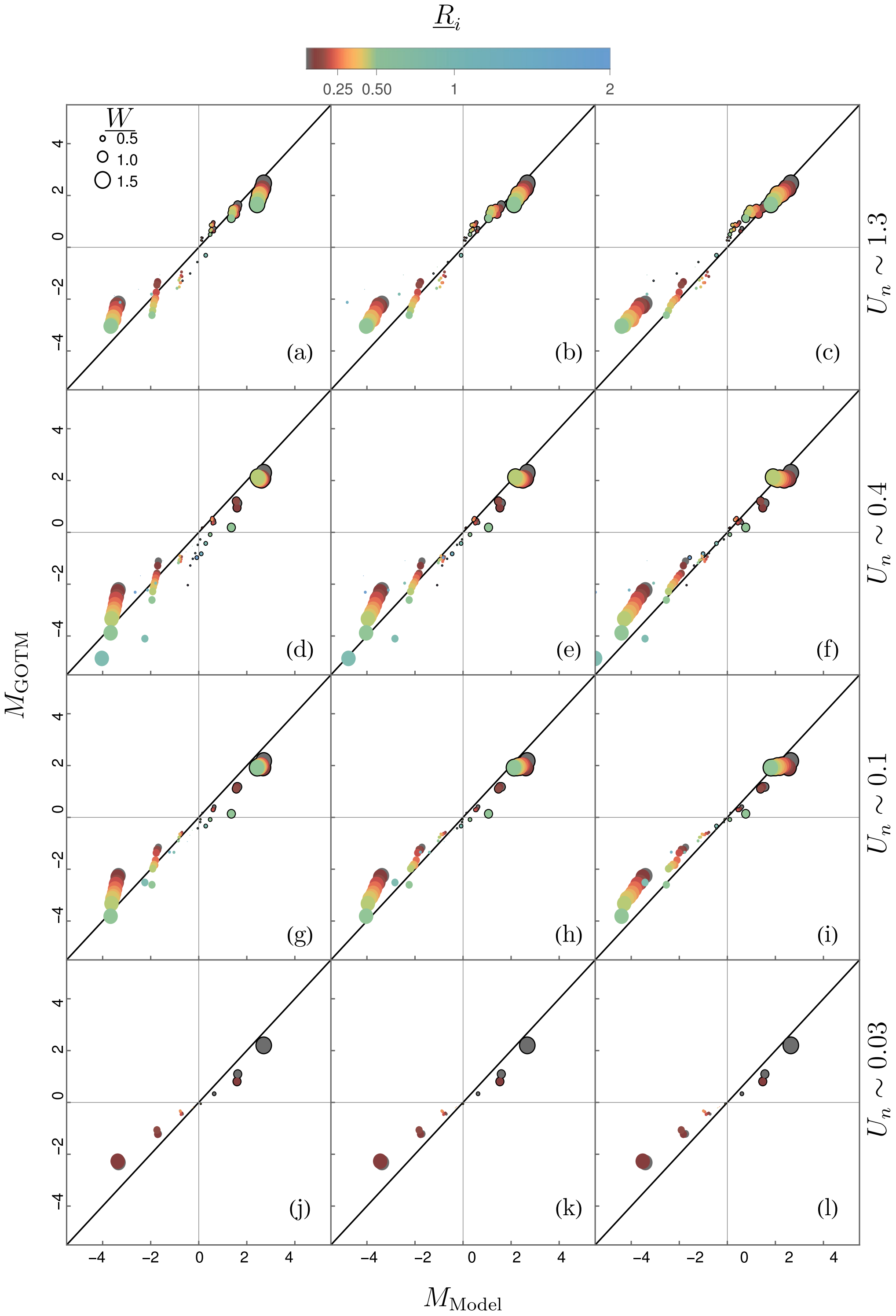

Fig. 9. Exchange flow intensity comparison M_{MODEL} vs. M_{GOTM} with $\tilde{u}_r = 0$, $H = 10$ m. M_{MODEL} is calculated by modifying the relative contribution of gravitational component of the exchange flow: $\tilde{U}_g$ (a, d, g, j), $2\tilde{U}_g$ (b, e, h, k), and $3\tilde{U}_g$ (c, f, i, l). Marker size and color denote W(scale is in the inset of (a)) and R_i with up-estuarine winds shown in magenta circles.

change in the estuary where different mechanisms dominate the influence of wind on the estuarine salinity structure. Imposing an eddy viscosity profile that accounts for the dynamic link between the boundary layer and local characteristics to such models may help to explore yet-unexplored intermediate-regions of the regime.

Lastly, caution should be taken when using the parameterization for meandering estuaries, or estuaries with sharp changes of morphologic features. The tidal variation of the wind stress and the buoyancy gradient, wave breaking, and variety of instabilities are ignored in this study. The integration of the tidal changes in buoyancy and wind stress is underway; this will extend some of the applicability limitations.

8. Conclusion

The significance of surface entrainment driven by directional and axial wind forcing in contributing to the exchange flow was explored.

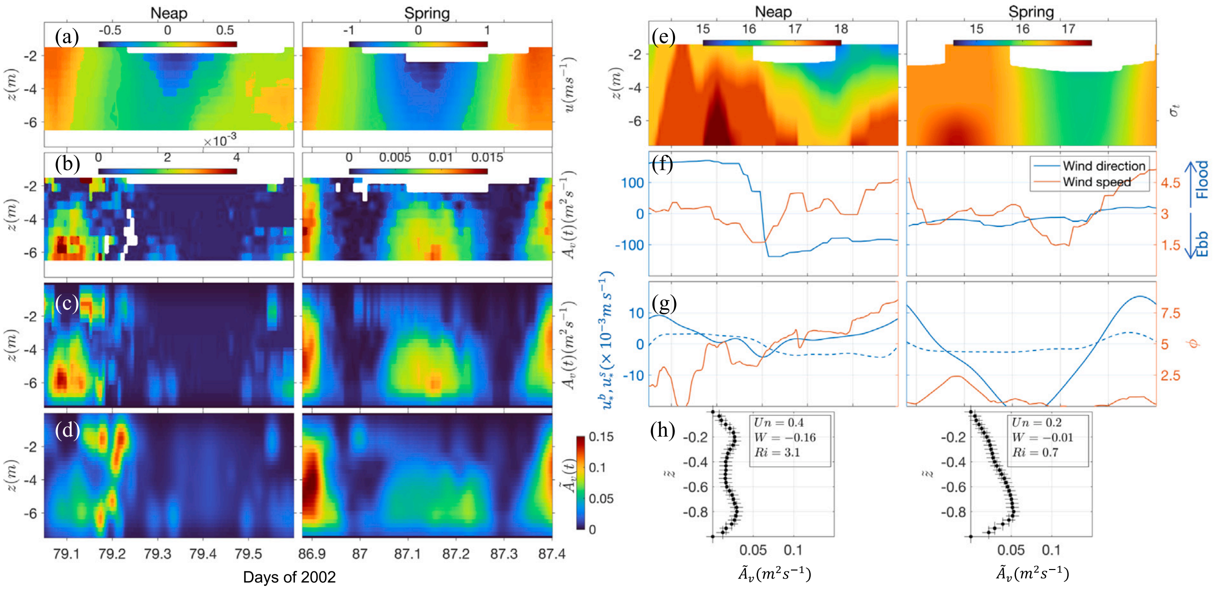

Fig. 10. Observations from the York River estuary, Virginia. (a) along-channel velocity, (b–d) tidal eddy viscosity, (e) density, (f) wind speed and direction, (g) surface (dashed) and bottom (solid) shear velocities and potential energy anomaly (red), and (h) tidally-averaged scaled eddy viscosity profiles for neap and spring tides (left and right panels, respectively). Data in (a, b, e, f) are adopted from Simpson et al. (2005); (c, d, g) and the state parameters in (h) are calculated using the bottom and surface stresses, vertical density, and horizontal density gradient. The tidal Av profiles in (c) are obtained by including the boundary values and interpolating to fill the data gaps in (b); the profiles are scaled by tidal bottom friction velocity and $H = 7.5$ m in (c). Bottom and surface roughnesses are z_0^b = 5E-5 and $z_0^s = 1400(u_*^s)^3/g$.

The eddy viscosity parameterization introduced in Part I (Basdurak et al., 2021) was extended to include wind entrainment and entrainment-driven bottom stress modifications. Tidally averaged relations were derived for surface and bottom boundary layer thicknesses, resulting in a novel parameterization of the A_v profile under both stable and unstable stratification. Co-varying boundary layer thicknesses were related to the exchange flow intensity and depths of flow infections.

The piecewise analytical solution for the exchange flow offers a simple yet robust way to explore a wide range of relevant dimensionless parameters as the typical runtime is in the order of seconds. Therefore, it is an idealized way to include the influence of wind.

Declaration of competing interest

The authors declare that they have no known competing financial interests or personal relationships that could have appeared to influence the work reported in this paper.

Data availability

Data will be made available on request.

Acknowledgments

The work of Hans Burchard was supported by the Collaborative Research Centre TRR 181 on Energy Transfers in Atmosphere and Ocean funded by the German Research Foundation (Project 274762653) and by the IOW Research Unit on Shallow Water Processes and Transition to Baltic Scale (STB). We thank the anonymous reviewers for their insightful comments and suggestions.

Appendix A. Eddy viscosity parameterization

In this appendix first the location of the A_v local-maxima will be derived in terms of the boundary layer thicknesses. Next the magnitudes of the A_v local-maxima are expressed as functions of these locations, roughness parameters and scaled wind stress. To achieve this, findings of previous observational studies and the tidally averaged GOTM output are used. Lastly, the parameterization for the upper A_v layer, i.e., A_v^I and A_v^S in (6), is given as a function of these local maxima characteristics.

A.1. Local-maxima depths of A_v, z_U and z_L

For the no-entrainment case, the location of the BBL peak z_L is found at $z_L = -H + h_b/2$, i.e., half the BBL thickness above the bed (Basdurak et al., 2021; see also Fig. 1a, e) with the h_b related to vertical stratification. Here, we adopt the same approach for the entrainment case to get the location of the BBL (Fig. 1c–d–e). For unstable conditions (illustrated in Fig. 2d), the tidally averaged A_v profiles obtained by GOTM show that the local maxima is found at or close to the mid-depth (Fig. A1d, upper panel; Fig. 1f); thus $z_L = z_U = -H/2$ i.e., as in fully-mixed water column without wind-entrainment (Fig. 1e). Three layers are distinguished when $z_U \neq z_L$ and $0 < h_b, h_s < H$ (Fig. 1c, d). For stable conditions the observational and numerical studies suggest that near-surface peak sensitively depends on wind induced stratification and interfacial shear due to varying BBL, and that the $|z_U|/h_s$ ratio is not constant. To parameterize z_U, the structure of the surface stress driven turbulent SBL described by Trowbridge (1992) is modified to account for the influence of the BBL mixing.

In this paper, three layers are distinguished: (I) wall region where boundary-generated turbulence dominates mixing with weak effects of stratification, (II) a region at marginal state in which turbulent mixing is just strong enough to maintain R_i near a critical value, and (III) a relatively narrow region where the Reynolds and Peclet numbers are large, so that molecular processes have a negligible effect on the Reynolds-averaged motion. The location of the SBL maximum is considered as the transition between regions (I) and (II). In the absence of the BBL mixing, Trowbridge (1992) estimated the scaled thickness of the wall region as $|z_U|/h_s \sim R_{i*}^{-1/4}$ where $R_{i*} = (N_0 h_s/u_*^s)^2$ is a bulk Richardson number based on the surface shear velocity and h_s. When both the BBL and SBL mixing are present, R_{i*} should scale with a length scale associated with the transition between the two layers h_i, and a velocity scale that considers both bottom and surface shears i.e., $(u_*^s)^2 + (u_*^b)^2$. When wind-driven waves are ignored, this extent of the transition from the dominant production of TKE by the wind stress log-layer to the bed stress log- layer can be determined by the relative size of the bed stress to the surface stress (Jones and Monismith, 2007). Motivated by the theoretical and observational findings and using the tidally averaged GOTM output for merging boundary layers, an explicit relation is found for $|z_U|$:

$$|z_U| = \left[\frac{h_s}{\left(0.75\sqrt[4]{R_{i*}^{\,s}},\ 1.5\right)_{\max}},\ \frac{H}{2} \right]_{\min}, \tag{A.1a}$$

$$R_{i*}^{\,s} = \frac{N^2 H h_i}{(u_*^s)^2 + (u_*^b)^2} \text{ and } \frac{h_i}{H} = 1 - \frac{1}{1 + |W|^{1.5}}. \tag{A.1b}$$

Here, h_i is expressed in terms of the state parameter W and (A.1a) is valid for $|W| > 0$. The h_i varies between $h_i \to 0$ when $u_*^s \ll u_*^b$ and $h_i \to H$ when $u_*^s \gg u_*^b$; it specifies the inflection point of the intermediate layer measured from the surface (e.g., when $|W| = 1$, the h_i equals the mid-depth; the A_V^I-dent in Fig. 1c). In (A.1a), $|z_U|$ is related to h_i via $R_{i*}^{\,s}$ by substituting N (9b) for N_0. The coefficient 0.75 is based on the comparison of the $h_s/|z_U|$ ratios, one calculated as a function of $\sqrt[4]{R_{i*}^{\,s}}$ and the other obtained by scaling (9) with z_U (via the A_v peak detection method).

The performance of (A.1a) is reasonable in predicting the $h_s/|z_U|$ ratio (Fig. A.1f). Without the constraints defined in (A.1a), when $R_{i*}^{\,s} \to 0$ the $|z_U| \to \infty$, similarly cases of $|z_U| \to 0$ may emerge. To avoid these, two constraints are used. The denominator of (A.1a) is constrained by theoretical findings; we adopt the bulk shear Richardson number maximum $R_{i*} = 16$ of Jones and Monismith (2007) model that captured the marginal state for the interfacial layer, yielding $0.75\sqrt[4]{16} = 1.5$. In the GOTM runs, the total water column depth is prescribed as relatively shallow to allow for the BBL and SBL simultaneously affecting the A_v. Thus, the upper limit for the $|z_U|$ is set to $H/2$ i.e., for a fully mixed water $|z_U| + |z_L| = H$.

A.2. Local-maxima depths of A_v, f_s and f_b

Local maxima magnitudes of the BBL and SBL, namely f_b and f_s are given by

$$f_b = \begin{cases} f_s^m & W > 1,\ h_s = h_b = H, \\ f_b^m & W \le 1,\ h_s = h_b = H, \\ f_b^0 & \text{otherwise}, \end{cases} \tag{A.2a}$$

$$f_s = \begin{cases} f_s^m & W > 1,\ h_s = h_b = H, \\ f_b^m & W \le 1,\ h_s = h_b = H, \\ \left[f_s^m,\ f_s^0\right]_{\min} & W > 1,\ (h_s, h_b) < H, \\ \left[f_b^m,\ f_s^0\right]_{\min} & W \le 1,\ (h_s, h_b) < H, \end{cases} \tag{A.2b}$$

$$\text{with } f_b^0 = \kappa u_*^b \frac{\left(H + z_L + z_0^b\right)^2}{2H + 2z_L + z_0^b}$$

$$\text{and} \quad f_s^0 = \begin{cases} f_b^0 \sqrt{|W|} \frac{-z_U}{z_L + H} & \mathcal{O}(h_s) \sim \mathcal{O}(h_b). \\ \kappa u_*^s \frac{\left(-z_U + z_0^s\right)^2}{h_s + z_0^s} & h_s \gg h_b \text{ or } h_b = 0. \end{cases} \tag{A.2c}$$

These relations are derived using the tidally averaged GOTM output. The upper limit for each maximum is defined separately as $f_b^m = f_b^0(z_L = {}^{-H}\!/2) \sim \kappa u_*^b H/4$ when $h_b = H$, and $f_s^m = f_s^0(z_U = {}^{-H}\!/2) \sim \kappa u_*^s H/4$ when $h_s = H$, assuming $(z_0^b, z_0^s) \ll H$. When the water column is well mixed due to either surface or bottom entrainment, the eddy viscosity maximum adjusts to f_s^m or f_b^m depending on the magnitude and direction of W (e.g., first two conditions shown in (A2a,b)). Here, $W = 1$ is set as a threshold for the wind-adjustment of the local maxima in each layer (BBL and SBL) based on the numerical model results. For up-estuarine wind shear dominating the bottom shear ($W > 1$), an unstably mixed ($R_f < 0$ and $\phi < 0$) water column (Fig. 2 top panel pinkish dots; bottom panel empty circles). Accordingly, the A_v^L parameterization in (7) is adjusted for a fully-mixed water column ($h_b = H$) when $W > 1$ with $d_0 = 0.5(1 - f_s^m/f_b^m) \sim 0.5(1 - u_*^s/u_*^b)$ ($d_0 = 0$ when $W \le 1$).

Eq. (A.2c) is used in ((A.2)a, b) when $(h_s, h_b) < H$. The relation for the BBL maximum f_b^0 is the same as in Basdurak et al. (2021). For the SBL, the maximum f_s equals f_s^0 when $h_s \gg h_b$ or in case of wind-entrainment only ($h_b = 0$), as in Fig. 1b (this condition emerges from the nature of parabolic wall-layer). However, for the cases when the BBL and SBL thicknesses are of the same order of magnitude (the first condition in (A.2c), Fig. 1c, d), the SBL has to be written as a function of both z_U and z_L. When $|W| = 1$ and $z_L + z_U = -H$, this expression is identical to the BBL maximum, $f_s^0 = f_b^0$.

Magnitude of the local maximum of $\tilde{A}_v = A_v/u_*^b H$ is shown in Fig. A.1a–c. Regardless of U_n, the up-estuarine winds yield bigger $(\tilde{A}_v)_{\max}$ magnitudes particularly for $|W| > 1$. Additionally there is an asymmetry in magnitudes with respect to We such that $(\tilde{A}_v)_{\max}$ increases with up-estuarine $|We|$, but first decreases then increases with down-estuarine $|We|$. This asymmetry intensifies as S_i increases. Peak positions on the other hand are symmetric with respect to $W = 0$ (Fig. A.1d). The $\tilde{A}_v$ profiles are grouped into single peaks (in SBL or BBL) and double peaks (in SBL and BBL) for stable conditions. As $|W|$ increases the profiles become parabolic with peaks appearing at the mid-depth. With increasing horizontal stratification, peaks appear near the boundaries. The SBL shallows with decreasing $|W|$ whereas the BBL first shallows then deepens around $|W| = 1$ due to high tidal amplitudes. Unstable conditions are linked to the merging boundary layers at mid-depth i.e., parabolic profiles but with magnitudes of $(\tilde{A}_v)_{\max} > 0.1$ because $u_*^s > u_*^b$.

Eq. (A.2) is compared to the eddy coefficients at the SBL and BBL peaks (Fig. A.1e); it performs well in predicting the A_v magnitudes particularly at the surface layer for both stable and unstable conditions. The discrepancies are less than an order of magnitude which is an improvement over the current approximations in the literature.

A.3. The upper layer A_v^U

With surface entrainment, a boundary layer develops in the water column near the surface, the so called surface boundary layer (SBL) in addition to the existing BBL. In case of strong enough wind stress (relative to the bottom stress), this surface layer also affects the bottom layer leading to changes in the BBL thickness and the mixing profile of the water column. Depending on the three state parameters (unsteadiness U_n, scaled wind stress W, and vertical stratification ϕ) the boundary layers either merge or stay apart. Moreover up-estuarine winds can destabilize the water column resulting in enhanced mixing coefficients. To describe all these different eddy viscosity profiles associated with surface entrainment, the general form of A_v^U should allow for both a single and a double layer profile in the upper part of the water column describing the surface and intermediate layers, A_v^S and A_v^I given in (6). Given the physical parameters that characterize the eddy viscosity profile e.g., boundary layer thicknesses (9), (10), local maxima magnitudes and depths (A.1a), (A.2), and with $h_I = z_U - z_L$, such a parameterization reads

$$A_v^U = \begin{cases} F_1 \varsigma\left(z, h_s\right) + f_S, \\ \qquad h_s = h_b = H \text{ or } h_I \le H/5, \\ (f_b - f_S)\, G(z) + \mathcal{H}\left(z - z_L\right)\left[F_1 \varsigma\left(z, -z_L\right) + f_S\right], \\ \qquad 0 < h_{s,b} \ne H \text{ and } H \le h_s + h_b < 2H, \\ F_0\, G(z) + \mathcal{H}\left(z - z_2\right)\ F_1 \varsigma\left(z, h_s\right) + f_S, \\ \qquad h_s = 0 \text{ or } h_b = 0 \text{ or } h_s + h_b < H, \end{cases} \tag{A.3a}$$

$$\text{with } G(z) = \prod_{z_L, z_1} (z)\, \zeta(z - z_U, \alpha, z_U - z_L), \tag{A.3b}$$

$$\varsigma(z, h) = \mathcal{H}\left(z - z_U\right) \zeta\left(z, 2, -z_U\right) + \prod_{z_L, z_U} (z)\, \zeta\left(-1 - z/h, 5, 1 + z_U/h\right), \tag{A.3c}$$

$$\text{and } \zeta(z, \alpha, h) = \left(-\frac{z}{h}\right)^{\alpha - 1} \left(\frac{H + z}{H - h}\right)^{(\alpha-1)(H/h-1)}. \tag{A.3d}$$

In (A3a), F_0, F_1 (Table A.1) are functions of the A_v-magnitudes at the local maxima f_b, f_s (A.2) and at the surface and bottom $f_S = A_v^U(z = 0)$

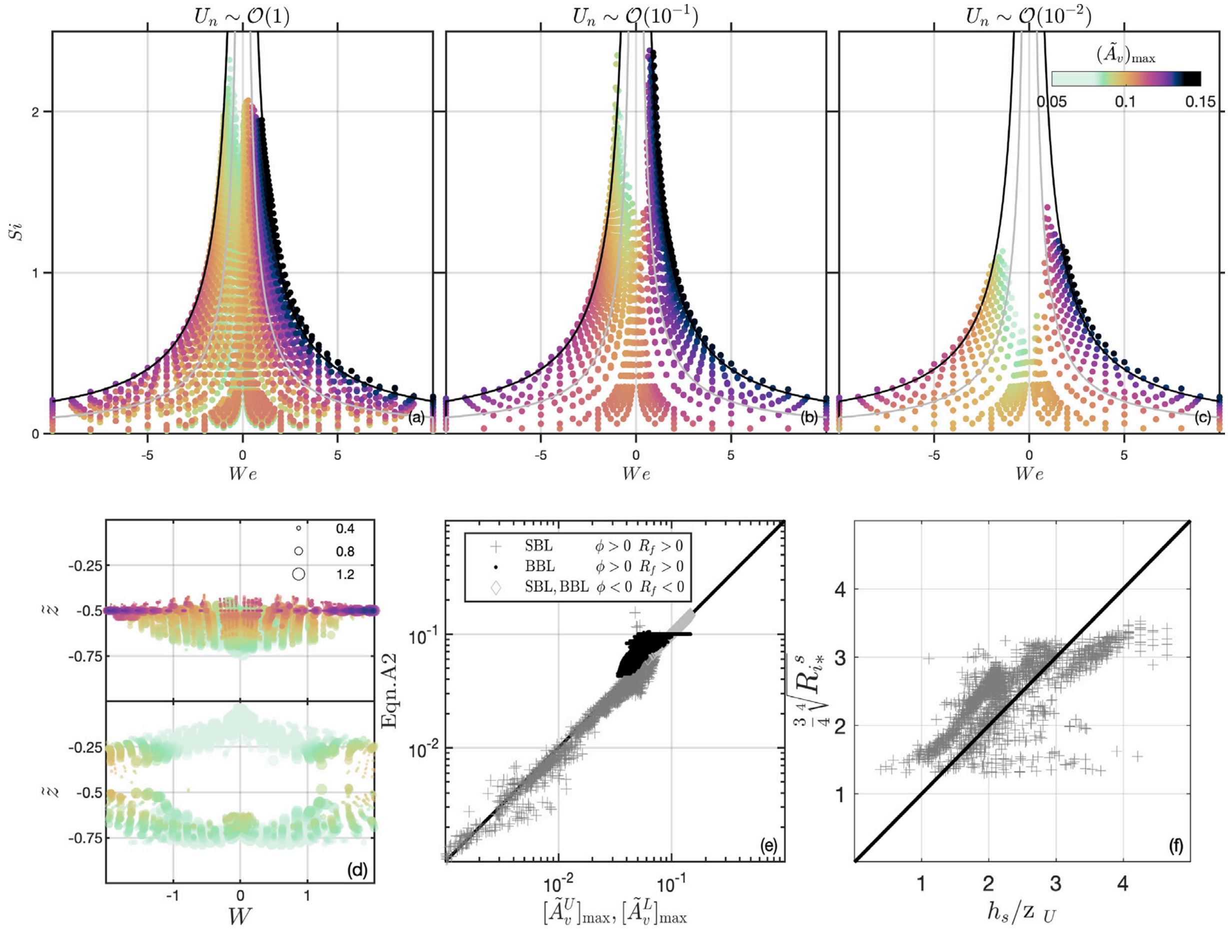

Fig. A.1. (a–c) As in Fig. 02 but for the depth−maximum of the scaled eddy−viscosity. (d) Scaled A_v-peaks and their vertical positions in the water column: (top panel) single peaks at, above, or below the mid-depth and (bottom panel) double peaks (below and above the mid-depth) for stable conditions. Marker size denotes U_n; its scale is referenced at the top-right corner. For unstable conditions A_v-peaks occur at the mid-depth. Approximations of (e) A_v-maxima for stable and unstable conditions and (f) near surface A_v-maximum location relative to the SBL thickness h_s/D_U for stable conditions; for unstable conditions $h_s = 2D_U \sim 2D_L$.

Table A.1
Relevant variables of A_v as illustrated in Fig. 1.

Case	z_1	z_2	F_0	F_1	α
Surface entrainment only (SBL)	$-h_s$	$-h_s$	$f_B - f_S$	$f_s + f_B - f_S$	5
Entrainment (BBL & SBL)	z_U	$-h_s$	f_b	$f_s - f_S$	5
No surface entrainment (BBL)	z_0^s	z_L	$f_b - f_S$	0	$\alpha(R_i)$
Entrainment (fully-mixed; BBL or SBL)	–	–	–	$f_b - f_S$	2

and $f_B = A_v^L(z = -H)$. The latter two are defined as $f_S = \kappa|u_*^s|z_0^s$ and $f_B = \kappa|u_*^b|z_0^b$ when $d_0 = 0$, and $f_B = \kappa(|u_*^b| + |u_*^s|)z_0^b/2$ when $d_0 \neq 0$ (i.e., when up-estuarine wind shear exceeds the bottom shear as described in Appendix A.2). The A_v^U profile is formed using the step functions $\mathcal{H}$, Π and the shape functions ζ, ς that are associated with the variables z_1, z_2 (defined in Table A.1) that set the limits for these functions. The discrete Heaviside function $\mathcal{H}(z - z_1)$ equals 0 when $z < z_1$, and 1 when $z \geq z_1$. The unit step (boxcar) function $\prod_{z_L, z_U}(z) = \mathcal{H}\left(z - z_L\right) - \mathcal{H}\left(z - z_U\right)$ equals 1 when $z_L \leq z \leq z_U$.

The shape function ζ given in ((A.3d)) is used to describe the profiles in each layer individually with the curvature parameter α (=2, 5 or $f(R_i)$) and the length scale h that set the degree of the curves and their limits, respectively. In (A.3b), ζ is used to describe the transition within the A_v^U profile i.e., within $z_L \leq z \leq z_U$ (surface entrainment) and $z_L \leq z \leq 0$ (no surface entrainment). The shape function ς in (A.3a)–(A.3c) is a joined function that consists of quadratic and a fifth degree ζ. These shape functions are used in such a way that the sign of curvature can vary depending on the layer under consideration (e.g., ς in (A.3c) with positive curvature for A_v^S and negative for A_v^I in case of a wind-entrainment; blue and purple lines in Fig. 1b). When the limits of the boxcar function are the same ($z_U = z_L$), the second part of (A.3c) drops and ς describes the A_v^S-shape only.

Rather than expressing the surface and intermediate layers separately for each case (Fig. 1), (A.3) is written as a conditional relation. The general form of A_v^U is based on three basic relations between h_s and h_b, and h_I. Here, h_I denotes the distance between the local maxima (e.g., the intermediate layer thickness); it is used to avoid a sharp layer transition between the two wall-layers. Each condition of (A.3a) is listed below (coefficients associated with (A.3) are given in Table A.1) with their special cases arising from relative thicknesses of the SBL and BBL.

- Mixed water column ($h_s = H$ or $h_b = H$ or $h_I \leq H/5$): The intermediate layer disappears and the A_v profile becomes parabolic i.e., bottom and surface wall layers A_v^S and A_v^L with a mid-depth local maximum (Fig. 1e, f). With $z_U = z_L = -H/2$ yielding $\prod_{z_L, z_L}(z) = 0$ and $\mathcal{H}\left(z \geq z_L\right) = 1$, the ς reduces to a parabolic shape function. This condition also applies for the local maxima positions that are too close to the mid-depth; hence the sharp curvatures are avoided by setting a threshold value for the intermediate layer thickness i.e., when $h_I \leq H/5$.
- Entrainment ($0 < h_{s,b} \neq H$ and $H \leq h_s + h_b < 2H$): This condition describes a stratified water column influenced by both the SBL and BBL mixing. The boundary layers partially merge with local A_v-maxima converging in magnitude towards each other (Fig. 1c, d:Type I). The profiles differ depending on the

relative magnitude of the local maxima; this is set by $h = H - hb/2$.

- Entrainment ($h_s + h_b < H$ when $h_{s,b} > 0$): This is the general form of the last condition in (A.3a) describing a stratified column influenced by both the SBL and BBL mixing but with fully-isolated local A_v-maxima (Fig. 1d:Type II). Magnitudes of each A_v-maximum converges to f_S and $h = h_s$. The following two cases emerge from the last condition of (A.3a) depicting only-surface and only-bottom entrainment cases.
- Surface entrainment only ($h_s + hb < H$ when $h_b = 0$): Without the bottom entrainment ($h_b = 0$ and $z_L = -H$) entrainment and $z_1 = z_2 = -h_s$ (Table A.1), the A_v^U profile can describe the full water column profile ($h_s \to H$); it consists of a wall-layer at the surface and a layer of marginal state (Fig. 1b). Consistent with the bottom boundary condition $A_v^L(z = -H, h_b = 0) = f_B$, the SBL maximum converges to f_B at $z = -h_s$ such that $A_v^U(z = -h_s) = f_B$ (Fig. 1b).
- No-surface entrainment ($h_s + hb < H$ when $h_s = 0$): With $F_1 = 0$, $\alpha(R_i) = erf(5R_i - 2.5) + 3$, $h_s = z_U = 0$ and associated step function limits (Table A.1), the (A.3) becomes identical to the A_v parameterization defined in Basdurak et al. (2021) i.e., a single layer $A_v^U(z = 0) = f_S$ (Fig. 1a).

The (6, A3) and its first derivative are continuous over depth. The continuity is satisfied because the vertical gradients at the local maxima are zero $\partial_z A_v|_{z=z_U} = 0$ and $\partial_z A_v|_{z=z_L} = 0$, and each layer has identical magnitudes at these locations.

Appendix B. Wind entrainment and stratification

When winds are weak and the surface entrainment rate is ignored, the bulk Richardson number R_i^0 can be used as a measure of vertical stratification (Basdurak et al., 2021). However, in the case of significant wind entrainment, a SBL develops and interacts with the BBL, affecting internal layers of the water column. Aforementioned ϕ (5), offers a better representation of vertical stratification than R_i^0, because it considers the density variance between internal layers of the water column. In this study, $\tilde{\phi} = \phi/[\rho_0 (u_*^b)^2]$ is used to quantify stratification. In this appendix, using the numerical model output, relations for R_i and S_i are derived in terms of $\tilde{\phi}$. The former is used in finding the BBL thickness in (10) and obtaining the A_v profiles (6), (A.3); the latter is used in analytically solving (11) for the exchange flow profiles.

B.1. Vertical stratification

One can obtain a measure for the wind adjusted vertical stratification using the turbulent output of the GOTM runs, and calculating tidally averaged Fr^{-2} with $Fr = \epsilon (tke|N|)^{-1}$ the turbulent Froude number. Before tidally and depth averaging, the range of Fr is restricted to $[0.01 - 20]$ based on the observational studies in estuaries. Consistent with Fr^{-2}, the wind adjusted vertical stratification R_i is approximated as a function of $\tilde{\phi}$ and W, both of which play a key role in modifying it:

$$R_i = [s_1 F(W) \tilde{\phi}^{s_2},\ 5] \quad \text{with} \quad F(W) = 1 - 0.85 \tanh(2\sqrt{|W|}), \tag{B.1}$$

with the constants $(s_1, s_2) = (1, 0.5)$ and $(s_1, s_2) = (20, 1)$ for stable and unstable conditions, respectively; it is constrained by $R_i = 5$ which denotes the fully-stratified conditions based on the direct numerical simulation studies of stably stratified fluids. In Fig. B.1a the numerically obtained vertical stratification Fr^{-2} is compared to (B.1). Except for the under-predictions of stable cases with $W < 0.5$ (i.e., bottom shear is more than twice the surface shear), R_i agrees well with Fr^{-2}. Hence, given the $\tilde{\phi}$ and W, one can obtain a wind-adjusted bulk vertical stratification without using a numerical model.

B.2. Horizontal stratification

Based on the relation between the numerically obtained and wind-adjusted stratification in horizontal and vertical directions (GOTM output), S_i can be related to R_i (B.1), and thus to $\tilde{\phi}$:

$$S_i = \left[0.35 \frac{R_i}{F(W)},\ 4\right]_{\min}. \tag{B.2}$$

The upper limit $S_i = 4$ is defined in Basdurak et al. (2021); (B.2) can be simplified by substituting $F(W)$ defined in (B.1), resulting in a $\tilde{\phi}$-dependent approximation for S_i. Changes of numerically-obtained S_i and approximated S_i (B.2) with Fr^{-2} are shown in Fig. B.1b and Fig. B.1c, respectively. The comparison shows that the S_i estimates (Fig. B.1c) are in good agreement with the model output (Fig. B.1b), for both stably and unstably stratified cases.

Appendix C. Piecewise solution

The A_v profile given in (6) depends on the following parameters: boundary layer thicknesses, local maxima locations and magnitudes. These parameters are obtained using the state parameters with relations given in Appendix A, B, and the variables ϕ, U_T, τ_s, z_0^s, and z_0^b. A flowchart describing the approach is shown in Fig. C.1b. In addition, a flowchart describing how R_i and S_i are linked to ϕ is separately shown in Fig. C.1a. With this, we have the depth and stratification dependent, physically driven A_v that reflects the changes induced by surface entrainment. Knowing the state variables, one can estimate the tidally averaged boundary layer thicknesses and eddy viscosity profile in an estuary where lateral advection and rotation effect is minimal, but tide and wind forcing is prominent. To solve for the exchange flow analytically (11), A_v^U needs to be approximated. As described in Basdurak et al. (2021), this is to avoid the fractional integrands in the shape functions arising from the non-polynomial ζ and ς (A.3c) and (A.3d). In the following section, we introduce polynomial and a combination of polynomial-exponential approximations of the A_v^U profile that still represent the original form accurately, but allow for analytical solutions.

C.1. Polynomial approximation of A_v^U

The upper eddy viscosity profile (A.3) is approximated as a polynomial by solving a system of equations that are expressed based on the vertical gradients and values of A_v^U at critical points that determine the shape of A_v^U (Appendix C of Basdurak et al. (2021) for a single upper layer without SBL). With a SBL, preset of the same approach is applied, however the set of constraints and the degree of approximations differ in case of $(h_s, h_b) < H$ when dual layers $(A_v^S), (A_v^I)$ are present (Fig. C.1c). Additionally, we assume that the SBL and BBL merges for cases of $h_I < 0.2H$ (i.e., minimum mid-layer thickness); this threshold is necessary to limit the extreme curvature for a quintic polynomial.

For A_v^S, the quadratic form is used (i.e., polynomial order $n = 2$ i.e., $A_v^S \approx p_2 z_z^2 + p_1 z + p_0$). To obtain the coefficients $p_0 \dots p_n$, $n + 1$ constraints have to be imposed. These three constraints are the values at $z_1 = 0$ and $z_2 = z_U$ and the zero gradient at $z_2 = z_U$.

$$\begin{bmatrix} z_1^2 & z_1 & z_1^0 \\ z_2^2 & z_2 & z_2^0 \\ 2z_2^1 & z_2^0 & 0 \end{bmatrix} \cdot \begin{bmatrix} p_2 \\ p_1 \\ p_0 \end{bmatrix} = \begin{bmatrix} A_v^S(z_1) \\ A_v^S(z_2) \\ \partial_z A_v^S(z_2) \end{bmatrix} \tag{C.1a}$$

For A_v^I, the quintic form ($n = 5$) is used which results in 6 unknown coefficients $\{p_0 \dots p_5\}$; the constraints to obtain these coefficients are

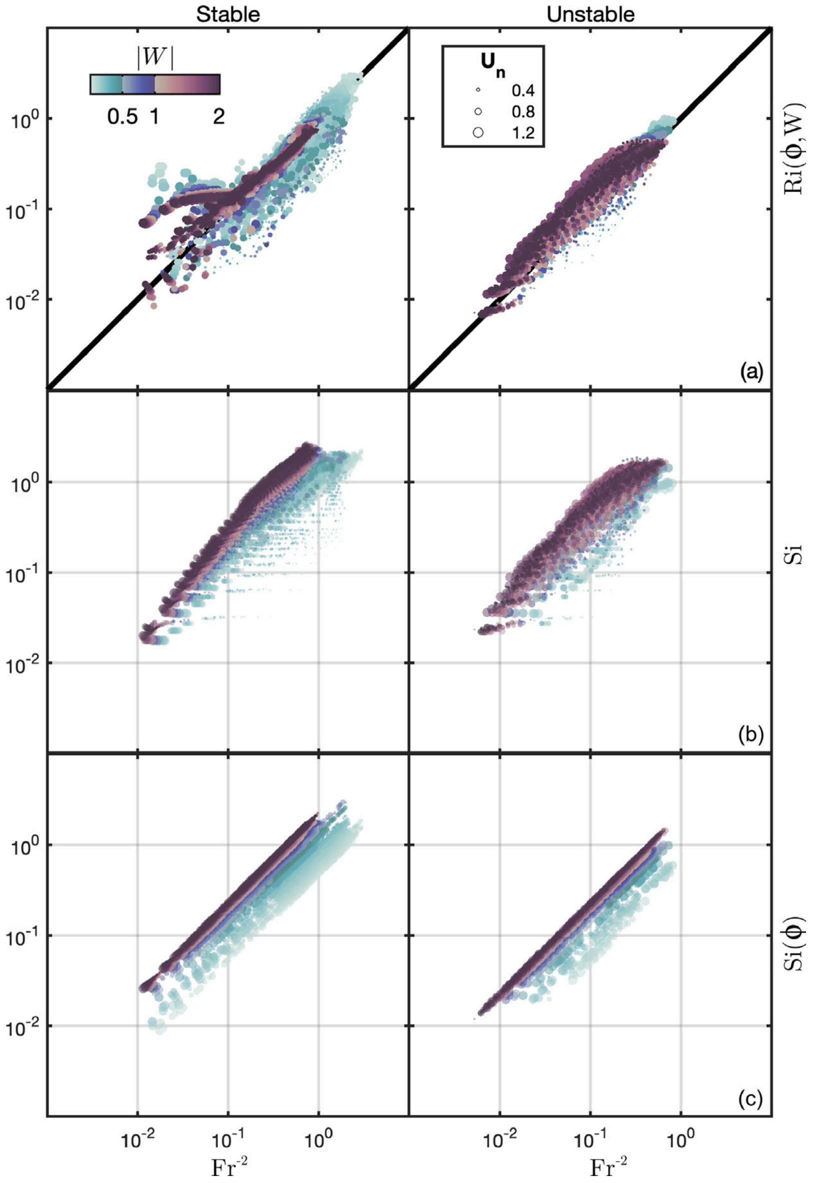

Fig. B.1. Tidally averaged bulk stratification relations derived using the GOTM output for stable and unstable conditions (left and right panels): Fr^{-2} vs. (a) R_i parameterization (B.1), (b) S_i obtained from GOTM, (c) S_i parameterization (B.2). Color denotes the scaled wind stress magnitude $|W|$; smaller circle sizes (smaller U_n) correspond to larger tidal amplitudes.

the values and gradients at $z_1 = z_U$, $z_2 = z_I$ and $z_3 = z_L$:

$$\begin{bmatrix} z_1^5 & \dots & z_1^0 \\ z_2^5 & \dots & z_2^0 \\ z_3^5 & \dots & z_3^0 \\ 5z_1^4 & \dots & 0 \\ 5z_2^4 & \dots & 0 \\ 5z_3^4 & \dots & 0 \end{bmatrix} \cdot \begin{bmatrix} p_5 \\ \vdots \\ p_0 \end{bmatrix} = \begin{bmatrix} A_v^I\left(z_1\right) \\ A_v^I\left(z_2\right) \\ A_v^I\left(z_3\right) \\ \partial_z A_v^I\left(z_1\right) \\ \partial_z A_v^I\left(z_2\right) \\ \partial_z A_v^I\left(z_3\right) \end{bmatrix}. \tag{C.1b}$$

The final form of A_v^I is found by optimizing the solution. This is achieved by adjusting the magnitude and location of the local minimum i.e., $A_v^I(z_I)$ and z_I, and minimizing the area between the curves of the parameterization (6) and the approximation. The minimization method is illustrated in Fig. C.1c ; this method requires solving (C.1b) over a mesh of $m_v \times m_z$ such that $z_2 = m_z z_I$ and $m_v A_v^U(z_I)$ with the mesh defined as:

$$m_v = \left\{ \frac{1}{10}\left[A_v^I\left(z_U\right), \frac{A_v^I(z_L)}{A_v^I(z_I)}\right]_{\min}, \dots, 1 \right\}, \quad m_z = \left\{ \frac{z_U+z_I}{2z_I}, \dots, \frac{z_L+z_I}{2z_I} \right\} \tag{C.1c}$$

The performance of the approximation is shown on Fig. 4. This approach makes the analytical solution possible (i.e., integer powers in the integrands, roots can be obtained for the reduced quintic form). This approximation performs well across the $W - U_n - R_i$ parameter space. In case of orders of magnitude reduction in A_v^I (e.g., Type II in Fig. 1d) with its vertical gradients approaching zero, an alternative method can be used to improve the polynomial approximation, which will be discussed in the following section.

C.2. Polynomial-exponential approximation of A_v^U

A hybrid approximation is used for the upper layer with different set of constraints for A_v^I and A_v^S (Fig. C.1d). This is achieved by first using an exponential function for A_v^I between $z_L \le z \le z_I = 2z_U$, then using a quintic polynomial for A_v^S between $z_I \le z \le 0$. Note that, although the surface and intermediate layer extents of the parameterization and the approximation differ, same values are used for local maxima locations and magnitudes as constraints. With constraint locations defined as

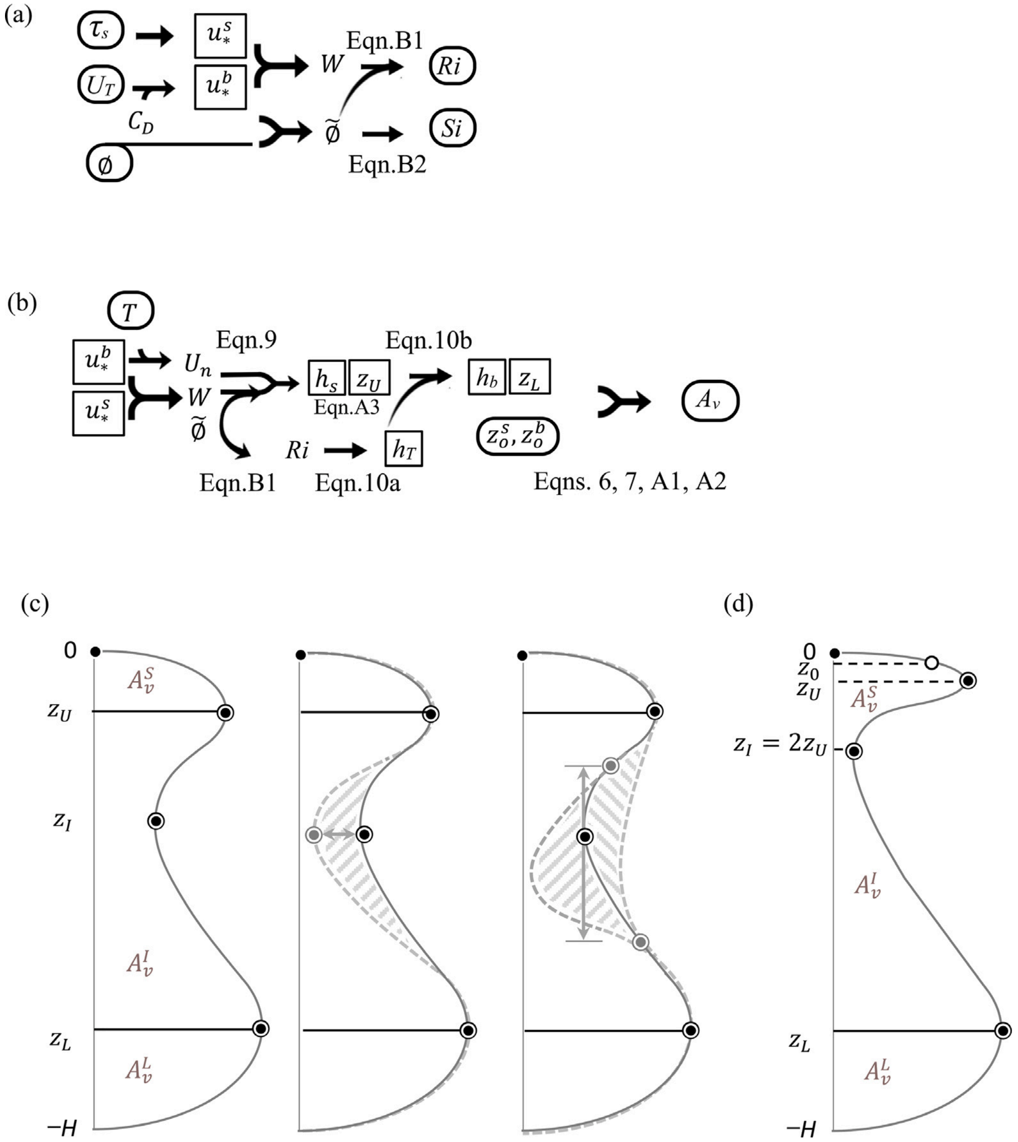

Fig. C.1. (a, b) A flowchart describing the procedure in calculating the tidally averaged parameters (a) R_i and S_i, (b) the A_v profile. (c) Polynomial approximation of the A_v^U profile; dashed gray line denotes the optimization of the approximation by adjusting z_I and minimizing the area (hatched space) between the parameterized and approximated profiles (d) Polynomial approximation of the A_v^S with exponential fit for A_v^I; note that extents of $A_v^{S,I}$ differ in (b) and (c). Layers are distinguished by black lines; z_I is the dip−location; circles (values) and filled markers (gradients) are the depth-continuity constraints for the approximation.

$z_1 = 0$, $z_2 = z_0 = -H/100$, $z_3 = z_U$ and $z_4 = 2z_U$, the set of equations to be solved for $\{p_0 \dots p_5\}$ to obtain A_v^S are:

$$\begin{bmatrix} z_1^5 & \dots & z_1^0 \\ z_2^5 & \dots & z_2^0 \\ z_3^5 & \dots & z_3^0 \\ z_4^5 & \dots & z_4^0 \\ 5z_3^4 & \dots & 0 \\ 5z_4^4 & \dots & 0 \end{bmatrix} \cdot \begin{bmatrix} p_5 \\ \vdots \\ p_0 \end{bmatrix} = \begin{bmatrix} A_v^S(z_1) \\ A_v^S(z_2) \\ A_v^S(z_3) \\ A_v^I(z_4) \\ \partial_z A_v^S(z_3) \\ \partial_z A_v^I(z_4) \end{bmatrix}, \tag{C.2a}$$

with A_v^I defined as:

$$A_v^I = Exp\left[ln\left(\frac{A_v(z_L)}{A_v(2z_U)}\right)\left(\frac{z - z_L}{2z_U - z_L}\right)^2 \right]. \tag{C.2b}$$

Appendix D. Analytical solution of exchange flow

Analogous to the solution described in Basdurak et al. (2021), the shape function γ in (11) is written for each A_v layer, and for each flow component. The two-layered form is the same as in Basdurak et al. (2021); it is applicable when either the boundary layer thicknesses scale with the water depth, or the local maximum of BBL and SBL are close enough to one another $z_U - z_L < 0.2H$ as discussed in Appendix C. The three-layered form can be expressed by including the mid layer: γ^U for $z_U \le z \le z_* = 0$, γ^I for $z_L \le z \le z_U$, γ^L for $-H \le z \le z_L$. Here $z_* = 0$, and this form can be reduced to two-layered form by adjusting its boundaries.

D.1. Sensitivity to A_v^U approximation

Exchange flow profiles resulting from different approximations are shown in Fig. D.1. For this, a set of state parameters that allow for

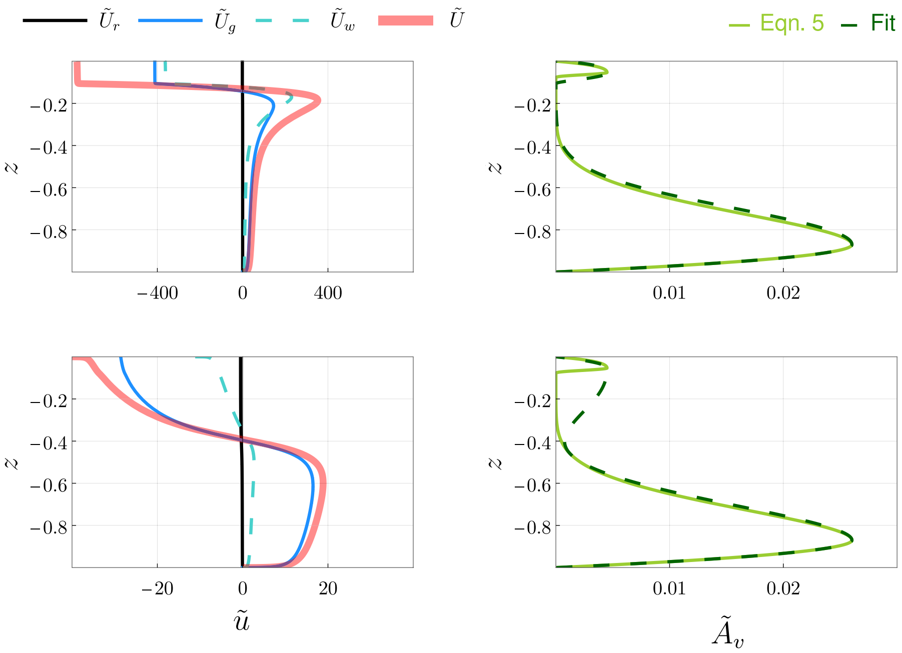

Fig. D.1. Exponential (top panel) vs. polynomial (bottom panel) fitting of interfacial $\tilde{A}_v$ layer to Eq. (5) between ($z_L \le z \le z_U$), and resulting exchange flow components for a fully stratified water column under weak wind and tidal forcing $S_i = 4, W = 0.1$, $U_n = 5$ and $\tilde{u}_r = -0.25$.

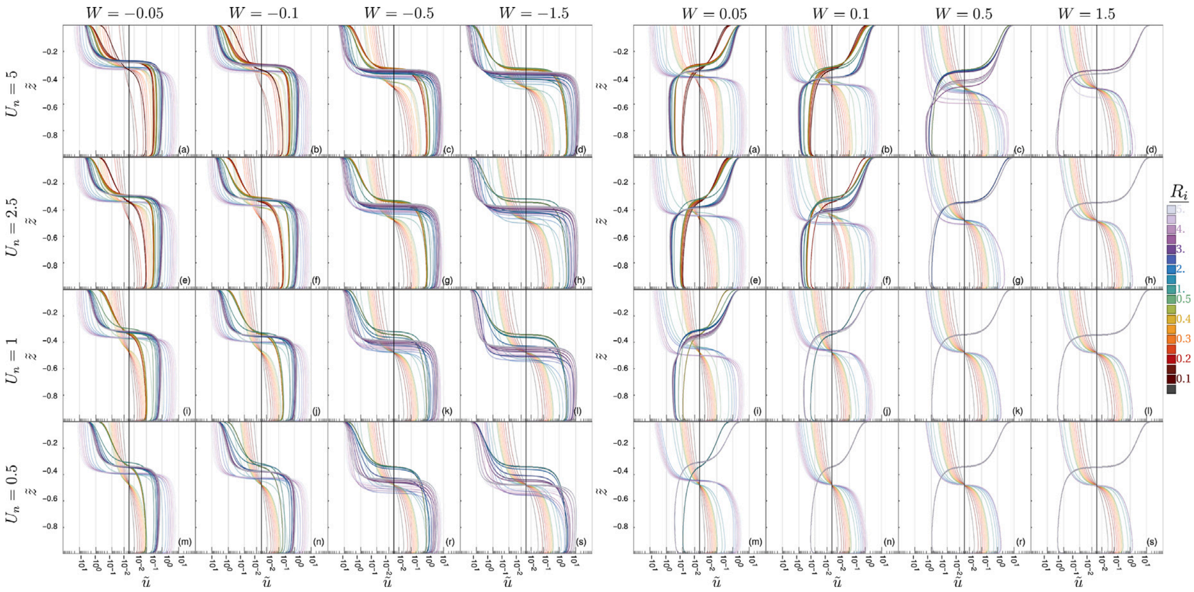

Fig. D.2. Sensitivity of the exchange flow components $\tilde{u}_g$ and $\tilde{u}_w$ (gravitational and wind-driven components for no-runoff cases) to $|W|$ (columns), U_n (rows) and R_i (transparent colors) for down-estuarine (a–s; left panel) and up-estuarine winds (a–s; right panel). Darker shades of colors are used for $\tilde{U}_w$ to distinguish from $\tilde{U}_g$. The profiles are obtained analytically using the polynomially approximated $\tilde{A}_v$-parameterization (dashed lines in Fig. 4). Note that the currents are shown on a logarithmic scale for a better visualization and that all the flow profiles converge to zero at the bottom of the water column.

more than an order of magnitude dip in the $\tilde{A}_v$ values (e.g., weak tides, weak winds, and fully-stratified water column), is chosen. Using only polynomial approximations for $\tilde{A}_v^U$ results in overestimation of the interfacial eddy viscosity coefficient that corresponds to milder exchange flow gradients (Fig. D.1, bottom panel). With exponential approximation, the interfacial shear of $\tilde{u}$ increases, and the exchange flow magnitudes increase by an order of magnitude with the return flow maximum occurring near the surface $z = -H/5$ (compared to $z = -H/2$, bottom panel).

D.2. Sensitivity of the flow components to R_i U_n and W

For no runoff cases $\tilde{u}_r = 0$, gravitational and wind driven components of the exchange flow are shown in Fig. D.2. One distinct feature that separates the wind driven component from the gravitational one is that, the inflection depths of the latter mostly occur at the mid-depth, except for strong stratification and weak winds (Fig. D.2a, e, i, m; both wind directions). Inflection depth of $\tilde{u}_w$ mostly occur above the mid-depth; its sensitivity to stratification increases with increasing

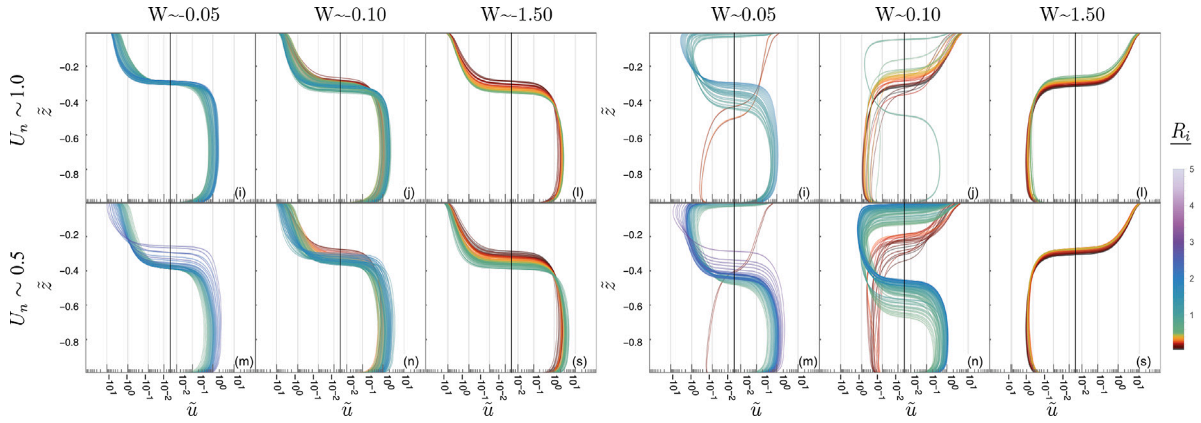

Fig. D.3. Same as in Fig. 6 but obtained from the GOTM simulations. Due to the GOTM constraints, a limited range of the parameter space is shown in comparison to Fig. 6 (lower two rows); only three columns from each panel (first, second and fourth columns of Fig. 6) are shown for visibility. The labeling (i, j, l, m, n, and s) and the colorspace is consistent with Fig. 6.

down-estuarine W and decreasing U_n (Fig. D.2s, left panel) that causes a thinner return flow. In up-estuarine direction wind driven component does not vary much with stratification for weaker U_n and stronger W (Fig. D.2s, right panel).

D.3. Comparison to the numerical solution

To compare the exchange flows resulting from the numerical model and the analytical model, the flow profiles obtained from GOTM runs are tidally-averaged, scaled and shown in the overlapping part of the parameter space of W, U_n, and R_i (Fig. D.3, consistent with Fig. 6). The simulations with runaway stratification are excluded. Additionally, for relatively high U_n or for weaker U_n with $R_i > 1$, GOTM does not converge to a periodic solution; these results are left out. The remaining GOTM profiles are grouped for unsteadiness ranges of $U_n \sim 0.5$, $U_n \sim 1$, and scaled wind stress ranges of $|W| \sim 0.05$, $|W| \sim 0.1$ and $|W| \sim 1.5$.

The numerical model compares well with the analytical model describing the down-estuarine driven two-layer flow and the up-estuarine driven stratified three-layer flow when the wind is weak or well-mixed two-layer flow (i, j, l, m, n, s of Fig. D.3, 6) except for some discrepancies. The results compare well when up-estuarine winds are stronger $W > 1$ (right panels; l, s of Fig. D.3, 6); when weaker, although the structure of the $\tilde{u}_{\mathrm{GOTM}}$ is similar to $\tilde{u}$, the intensity of the exchange shows discrepancies i.e., $|\tilde{u}_{\mathrm{GOTM}}| > \tilde{u}$ (right panels; i, j, m, n of Fig. D.3, 6). For weaker winds, stratification changes yield inconsistencies in the flow's inflection depths. For three-layered types, downwind flow occurs closer to the surface whereas the downwind part of the return flow occurs closer to mid-depths, which differs from the analytically obtained exchange profiles.

These inconsistencies may be related to the ESCO driven flows that are ignored in the analytical model (i.e., exchange flow contribution from the tidal covariance of vertical shear and eddy viscosity coefficient as discussed in Part I). This is further discussed in Section 5b.

References

Basdurak, N.B., Burchard, H., Schuttelaars, H.M., 2021. A local eddy viscosity parameterization for wind-driven estuarine exchange flow. Part I: Stratification dependence. Prog. Oceanogr. 193, 102548.

Burchard, H., 2009. Combined effects of wind, tide, and horizontal density gradients on stratification in estuaries and coastal seas. J. Phys. Oceanogr. 39 (9), 2117–2136.

Burchard, H., Bolding, K., Lange, X., Osadchiev, A., 2023. Decomposition of estuarine circulation and residual stratification under landfast sea ice. J. Phys. Oceanogr. 53 (1), 57–80.

Burchard, H., Hetland, R.D., 2010. Quantifying the contributions of tidal straining and gravitational circulation to residual circulation in periodically stratified tidal estuaries. J. Phys. Oceanogr. 40 (6), 1243–1262.

Burchard, H., Hetland, R.D., Schulz, E., Schuttelaars, H.M., 2011. Drivers of residual estuarine circulation in tidally energetic estuaries: Straight and irrotational channels with parabolic cross section. J. Phys. Oceanogr. 41 (3), 548–570.

Burchard, H., Petersen, O., Rippeth, T.P., 1998. Comparing the performance of the mellor-yamada and the κ-ϵ two-equation turbulence models. J. Geophys. Res.: Oceans 103 (C5), 10543–10554.

Chen, W., De Swart, H.E., 2016. Dynamic links between shape of the eddy viscosity profile and the vertical structure of tidal current amplitude in bays and estuaries. Ocean Dyn. 66 (3), 299–312.

Chen, S.-N., Sanford, L.P., 2009. Axial wind effects on stratification and longitudinal salt transport in an idealized, partially mixed estuary. J. Phys. Oceanogr. 39 (8), 1905–1920.

Cheng, P., de Swart, H.E., Valle-Levinson, A., 2013. Role of asymmetric tidal mixing in the subtidal dynamics of narrow estuaries. J. Geophys. Res.: Oceans 118 (5), 2623–2639.

Cheng, P., Valle-Levinson, A., de Swart, H.E., 2011. A numerical study of residual circulation induced by asymmetric tidal mixing in tidally dominated estuaries. J. Geophys. Res.: Oceans 116 (C1).

Deleersnijder, E., Luyten, P., 1994. On the practical advantages of the quasi-equilibrium version of the mellor and yamada level 2.5 turbulence closure applied to marine modelling. Appl. Math. Model. 18 (5), 281–287.

Dijkstra, Y.M., Schuttelaars, H.M., Burchard, H., 2017. Generation of exchange flows in estuaries by tidal and gravitational eddy viscosity-shear covariance (ESCO). J. Geophys. Res.: Oceans 122 (5), 4217–4237.

Geyer, W.R., 1997. Influence of wind on dynamics and flushing of shallow estuaries. Estuar. Coastal Shelf Sci. 44 (6), 713–722.

Hetland, R.D., Geyer, W.R., 2004. An idealized study of the structure of long, partially mixed estuaries. J. Phys. Oceanogr. 34 (12), 2677–2691.

Jones, N.L., Monismith, S.G., 2007. Measuring short-period wind waves in a tidally forced environment with a subsurface pressure gauge. Limnol. Oceanogr. Methods 5 (10), 317–327.

Jongbloed, H., Schuttelaars, H.M., Dijkstra, Y.M., Donkers, P.B., Hoitink, A.J., 2022. Influence of wind on subtidal salt intrusion and stratification in well-mixed and partially stratified estuaries. J. Phys. Oceanogr. 52 (12), 3139–3158.

Kato, H., Phillips, O., 1969. On the penetration of a turbulent layer into stratified fluid. J. Fluid Mech. 37 (4), 643–655.

Lange, X., Burchard, H., 2019. The relative importance of wind straining and gravitational forcing in driving exchange flows in tidally energetic estuaries. J. Phys. Oceanogr. 49 (3), 723–736.

Price, J.F., 1979. On the scaling of stress-driven entrainment experiments. J. Fluid Mech. 90 (3), 509–529.

Purkiani, K., Becherer, J., Klingbeil, K., Burchard, H., 2016. Wind-induced variability of estuarine circulation in a tidally energetic inlet with curvature. J. Geophys. Res.: Oceans 121 (5), 3261–3277.

Scully, M.E., Friedrichs, C., Brubaker, J., 2005. Control of estuarine stratification and mixing by wind-induced straining of the estuarine density field. Estuaries 28, 321–326.

Simpson, J.H., Brown, J., Matthews, J., Allen, G., 1990. Tidal straining, density currents, and stirring in the control of estuarine stratification. Estuaries 13 (2), 125–132.

Simpson, J.H., Williams, E., Brasseur, L.H., Brubaker, J.M., 2005. The impact of tidal straining on the cycle of turbulence in a partially stratified estuary. Cont. Shelf Res. 25 (1), 51–64.

Stacey, M.T., Brennan, M.L., Burau, J.R., Monismith, S.G., 2010. The tidally averaged momentum balance in a partially and periodically stratified estuary. J. Phys. Oceanogr. 40 (11), 2418–2434.

Trowbridge, J., 1992. A simple description of the deepening and structure of a stably stratified flow driven by a surface stress. J. Geophys. Res.: Oceans 97 (C10), 15529–15543.

Umlauf, L., Burchard, H., 2005. Second-order turbulence closure models for geophysical boundary layers. a review of recent work. Cont. Shelf Res. 25 (7–8), 795–827.

Verspecht, F., Rippeth, T., Howarth, M., Souza, A., Simpson, J., Burchard, H., 2009. Processes impacting on stratification in a region of freshwater influence: Application to liverpool bay. J. Geophys. Res.: Oceans 114 (C11).

Zitman, T.J., Schuttelaars, H.M., 2012. Importance of cross-channel bathymetry and eddy viscosity parameterisation in modelling estuarine flow. Ocean Dyn. 62 (4), 603–631.